PCCP

Accepted Manuscript

ROYAL SOCIETY OF CHEMISTRY

www.rsc.org/pccp

Effect of the electropositive elements A = Sc, La, and Ce on the microscopic dynamics of $A\mathbf{V}_2\mathbf{Al}_{20}$

Michael Marek Koza[1,2], Andreas Leithe-Jasper[2], Erik Sischka[2],
Walter Schnelle[2] Horst Borrmann[2], Hannu Mutka[1], Yuri Grin[2]
[1]*Institut Laue Langevin, 6 Rue Jules Horowitz,*
B.P. 156, 38042 Grenoble, Cedex 9, France.
[2]*Max–Planck–Institut für Chemische Physik fester Stoffe,*
Nöthnitzer Straße 40, 01187 Dresden, Germany.

(Dated: September 11, 2014)

Abstract

We report on the inelastic response of AV_2Al_{20} (with A = Sc, La and Ce) probed by high–resolution inelastic neutron scattering experiments. Intense signals associated with the dynamics of Sc, La and Ce are identified in the low–energy range at 6–14 meV in ScV_2Al_{20} and at 8–16 meV in LaV_2Al_{20} and CeV_2Al_{20}. Their response to temperature changes between 2 and 300 K reveals a very weak softening of the modes upon heating in LaV_2Al_{20} and CeV_2Al_{20} and a distinguished blue shift by about 2 meV in ScV_2Al_{20}. By means of density functional theory (DFT) and lattice dynamics calculations (LDC) we show that the unusual anharmonicity of the Sc–dominated modes is due to the local potential of Sc featured by a strong quartic term. The vibrational dynamics of ScV_2Al_{20} as well as of LaV_2Al_{20} and CeV_2Al_{20} is reproduced by a set of eigenmodes. To screen the validity of the DFT and LDC results they are confronted with data from x–ray diffraction measurements. The effect of the strong phonon renormalization in ScV_2Al_{20} on thermodynamic observables is computed on grounds of the LDC derived inelastic response. To set the data in a general context of AV_2Al_{20} compounds and their physical properties we report in addition computer and experimental results on the binary V_2Al_{20} compound.

I. INTRODUCTION

Crystalline compounds such as skutterudites (AT_4X_{12} with A = alkali, alkaline–earth, rare-earth, actinide metals or thallium, T = Fe, Ru, or Os, X = P, As, or Sb), silicon– and germanium–based clathrates, β–pyrochlore oxides ($A\mathrm{Os}_2\mathrm{O}_6$ with A = K, Rb, Cs) and $A\mathrm{V}_2\mathrm{Al}_{20}$ (with A = Al, Sc, Ga, Y, Lu, La, Ce), to name a few only, are formed by a network of interconnected polyhedra which features open voids and allows different electropositive elements A to be embedded into them.[1–3] In many of these compounds experiments established the presence of apparently localized vibrational modes at energies as low as a few millielectronvolts only, i.e. within the range of acoustic phonons.[4–17] Often, results from diffraction and bulk experiments on these compounds can be satisfactorily approximated by implying the existence of a low–energy Einstein mode. For this reason these compounds are often referred to as Einstein solids, a term applied originally to $\mathrm{Al}_x\mathrm{V}_2\mathrm{Al}_{20}$.[18] A few of these Einstein solids show an unusual response to temperature changes. Thereby, the low–energy modes exhibit a blue–shift upon heating and inspired to dub the blue–shifting excitations 'rattling' modes.[4,14,19–23]

Numerous experimental studies on the electronic and heat transport properties of Einstein solids indicate a distinguished interaction of the localized low–energy modes with electrons and phonons of the compounds. Low–energy modes facilitate Cooper–pairing and, thus, superconductivity in metals.[13,14,21,22,24–26] They form an obstruction to thermal transport accomplished by long wavelength phonons.[27–29] The last feature is being paid great attention to for its potential exploitation in thermoelectric devices whose materials require very low lattice thermal conductivities $\kappa_l(T)$ for excellent performance.

Over the past few years, microscopic experiments such as inelastic neutron scattering (INS) and dedicated simulation and modelling techniques have refined the perception of the localized low–energy vibrations. It is found that collective modes, i.e. phonons, can account for the properties of the low–energy inelastic response with high quality.[15,16,20,30–40] Weaker bonding of the electropositive elements with the polyhydral matrices results in rather low energies of their collective, hybrid modes. The formation of low–energy vibrational eigenmodes is as well facilitated by high masses of the elecropositive elements often used for the alloying. In any case the low–energy nodes are characterized by distinguished dispersion $\omega(\mathbf{Q})$, i.e. the energy $\hbar\omega(\mathbf{Q})$ of eigenstates varies strongly with their momentum $\hbar\mathbf{Q}$, and give rise to a number of van Hove singularities $\partial\omega(\mathbf{Q})/\partial\mathbf{Q} = 0$ at different $\mathbf{Q}$.[41–44] The van Hove singularities manifest themselves as multiple maxima in $\mathbf{Q}$–averaged inelastic responses such as the vibrational density of states $Z(\omega)$. Whereas in experiments probing momentum– and energy–averaged signals, such as heat capacity measurements and thermal displacement studies, they are settled as an apparent single Einstein frequency.[45–47]

The importance of the low–energy phonons for the lattice thermal conductivity is not completely clear since $\kappa_l(T)$ is modified strongly by other properties of the compounds. For example, topological and chemical disorder and partial filling of the voids are some dominant effects reducing $\kappa_l(T)$ significantly.[48–50] They are indeed common to and vary appreciabely in most of the Einstein solids listed above. To draw conclusions of general validity upon the effect of the low–energy 'rattling' modes on the thermal conductivity a compound has to be studied whose low–energy dynamics is known to be the primary impact on $\kappa_l(T)$ and can be tuned in a wide range of energies by the inclusion of distinct electropositive elements.

In this paper we discuss that $A\mathrm{V}_2\mathrm{Al}_{20}$ accepting a variaty of electropositive elements A such as Al, Sc, Ga, Y, Lu, La, Ce, Yb is a promising compound for such studies. The compounds $A\mathrm{V}_2\mathrm{Al}_{20}$ adopting the cubic $\mathrm{CeCr}_2\mathrm{Al}_{20}$ structure type which is sketched in Fig. 1 are built up by slightly distorted icosahedra formed by Al(48f) and Al(96g) (Wyckoff positions are given in parentheses) atoms surrounding V atoms. These icosahedra are linked together by the Al(48f) atoms along the [110] direction. Such inter–connected icosahedra form a tetrahedral framework with the Al(16c) atoms being in the center of hexagonal prisms. These prisms share common triangular faces with the icosahedra and are thus composed of Al(96g) atoms. In this architecture the A atoms reside in spacious voids occupying the (8a) position (see Fig. 1). They are coordinated by 12 Al(96g) atoms forming a truncated tetrahedron. Another 4 Al(16c) atoms cap the hexagonal faces of the truncated tetrahedron. This kind of coordination polyhedron with 16 vertices is called Friauf polyhedron and is frequently encountered in complex topologically close-packed intermetallic crystal structures.

The distinct dependence of $\kappa_l(T)$ on different filler atoms is highlighted in Fig. 2 which depicts experimental data on Sc and La containing $\mathrm{V}_2\mathrm{Al}_{20}$. The results demonstrate a strong suppression of $\kappa_l(T)$ in $\mathrm{ScV}_2\mathrm{Al}_{20}$ and indicate a peculiar temperature (T) dependence. Thereby $\kappa_l(T)$ is steadily increasing upon heating with no indication of a maximum as it is expected from a crystalline compound with a well defined Debye temperature (Θ_D).[41,42] To shed light on this peculiar property we probe the microscopic dynamics of $\mathrm{ScV}_2\mathrm{Al}_{20}$,

LaV_2Al_{20} and CeV_2Al_{20} by T–dependent INS experiments and identify their low–energy vibrational eigenmodes. We demonstrate that the T response of these eigenmodes is tuned from a rather classical anharmonic behaviour in LaV_2Al_{20} and CeV_2Al_{20}, i.e. red–shifting upon heating, to a 'rattling' like anharmonicity in ScV_2Al_{20}, i.e. blue–shifting upon heating.

The INS experiments are accomponied by x–ray diffraction on the series of Al, Sc, La and Ce containing AV_2Al_{20} and backed up by density functional theory (DFT), lattice dynamics calculations (LDC) and powder averaged lattice dynamics calculations (PALD) of AV_2Al_{20} with $A = \square$, Sc, La, and Ce. With $A = \square$ we refer throughout this paper to the computer generated binary compound with voids left unoccupied. To allow a close up view of the inelastic signal specific to the elecropositive elements their scattering power in INS requires to be sufficiently high. For this reason the focus is set onto the Sc and La containing compounds. The scattering power of Ce is small thus the signal in INS from CeV_2Al_{20} reflects the dynamics of the poly–anionic matrix, however, modified by the coupling with Ce.

II. EXPERIMENTS AND DENSITY FUNCTIONAL CALCULATIONS

A. Sample Preparation and Characterization

AV_2Al_{20} (A = Sc, La, Ce) samples of the ternary compounds were prepared by a multistep synthetic approach. First, binary precursor compounds VAl_3, $ScAl_3$, $LaAl_4$, and $CeAl_4$ were synthesized by arc melting from the elemental metals (Sc, ingots, Chempur 99.9 wt.%, La rods, Ames, 99.9 wt.%, Ce rods, Ames 99.9 wt.%). The binary compounds were placed in corundum crucibles, sealed in evacuated quartz ampoules and heat treated at 900°C for 5 days. After that they were ground in a hard–metal mortar to a fine powder (particle size $< 100\mu$m) which was then blended with Al powder in stoichiometric ratios following equation: $AAl_x + 2\ VAl_3 + (14 - x)Al \longrightarrow AV_2Al_{20}$.

Sample batches of $3g$ each were cold compacted in press forms without the use of lubricants. The resulting tablets were placed in corundum crucibles, sealed into quartz tubes under an atmosphere of about 400 mbar Ar gas. After slow heating to 600°C the samples were kept at this temperature for 1 week for an initial heat treatment. Then they were reground and re–compacted and annealed at temperatures of 700 to 750°C for one week.

These steps were repeated until reactions were completed.

The ternary compounds were obtained as dense sintered sample specimens. A minor impurity of free Al metal was detected by x–ray diffraction and microprobe analysis. Tiny crystals of $\mathrm{ScV_2Al_{20}}$ could be isolated from a sample with $\mathrm{ScV_2Al_{20}}$ composition prepared by arc melting from the elements, annealed at 660°C for one month, followed by heat treatment at 800°C for 1 week in a corundum crucible which was sealed into a quartz tube under an atmosphere of 400 mbar Ar gas.

Metallographic microstructure analyses on polished surfaces were performed with optical microscopy and electron probe microanalysis. The latter investigations were carried out with energy dispersive analysis (EDX) in a Philips XL 30 scanning electron microscope. The chemical compositions deduced by EDX analysis are: $\mathrm{Sc_{0.9(1)}V_2Al_{20}}$, $\mathrm{La_{0.9(1)}V_2Al_{20}}$, $\mathrm{Ce_{0.9(2)}V_2Al_{20}}$. Note, that for clarity we set aside the notion of the filling ratios throughout this paper.

B. X–ray Diffraction and Thermal Conductivity

Powder x-ray diffraction (XRD) measurements were made using CoKα radiation ($\lambda = 1.789007$ Å) applying the Guinier-Huber technique. Single crystal data of $\mathrm{ScV_2Al_{20}}$ and $\mathrm{Al_xV_2Al_{20}}$ were collected on a Rigaku R–axis RAPID diffractometer (Mo $\mathrm{K_\alpha}$, $\lambda = 0.71073$ Å). Crystallographic structure refinements and calculations were made with the WINCSD[51] and SHELXL-97[52] program packages. Achieved reliability factors[52] of the single crystal structure refinements are: $\mathrm{ScV_2Al_{20}}$ ($R_1 = 0.029$ for 246 $F_o > 4(Fo)$; $wR_2 = 0.051$). For the full profile powder refinements[51]: $\mathrm{LaV_2Al_{20}}$ (R intensity: 0.0517, 0.094), $\mathrm{CeV_2Al_{20}}$ (R intensity: 0.056, 0.099).

The thermal conductivity $\kappa(T)$ (see Fig. 2) was determined simultaneously with the electrical resistivity $\rho(T)$ and the Seebeck coefficient $S(T)$ with a commercial setup (option TTO, PPMS, Quantum Design). The lattice contribution to the thermal conductivity, $\kappa_l(T)$, was estimated by subtracting the conduction electron contribution κ_e from the total $\kappa(T)$. κ_e was estimated by the Wiedemann-Franz law with $L_0 = 3(\pi k_B/3e)^2 \approx 2.45 \times 10^{-8}$ J s^{-1} Ω K^{-1}.

C. Inelastic Neutron Scattering Experiments

INS experiments were carried out with the compounds ScV_2Al_{20}, LaV_2Al_{20}, and CeV_2Al_{20} at the time–of–flight spectrometers IN4@ILL and IN6@ILL located at the European neutron source Institut Laue Langevin in Grenoble, France. The cold–neutron spectrometer IN6@ILL was utilized in the time–focusing mode with best energy resolution set to 7.5 meV at the anti–Stokes line and the incident neutron wavelength $\lambda_\mathrm{i} = 4.14$ Å. The thermal–neutron spectrometer IN4@ILL was utilized in the elastic focusing mode, i.e. with best energy resolution set to 0 meV and two different λ_i. Both λ_i were chosen for best resolution of the low–energy modes in the studied compounds resulting in $\lambda_\mathrm{i} = 2.2$ Å for ScV_2Al_{20} and $\lambda_\mathrm{i} = 1.8$ Å for LaV_2Al_{20} and CeV_2Al_{20}.

Powdered specimen of the compounds of about 20 g each were measured at temperatures T between 2 and 300 K. We applied $T \approx 100$ and 300 K for all samples at IN6@ILL. At IN4@ILL ScV_2Al_{20} and LaV_2Al_{20} were measured at $T \approx 2, 50, 100, 200$ and 300 K whereas CeV_2Al_{20} was studied at 2, 70, 230 and 300 K. Precise T values are reported with the data hereafter. Standard procedures for data correction and conversion were utilized. Data are corrected for empty can scattering, for absorption, self–attenuation and frame overlap effects, for different detector efficiencies of the multidetector units, and for the energy dependence of the Helium–3 counters. Scattering lengths and absorption cross sections tabulated in the literature were exploited.[53] Their values are listed in table I.

The dynamic structure factors $S(\omega, T)$ were calculated as a scattering–angle averaged signal. To highlight the effect of the Debye–Waller factor (DWF) on the dynamic response functions the $S(\omega, T)$ are corrected for the Bose–Einstein thermal occupation number. The generalized density of states $G(\omega)$ was derived taking full account of the incoherent approximation formalism.[40,43,44,54,55]

D. *Ab Initio* Lattice Dynamics Calculation

First principle calculations were performed using the projector–augmented wave formalism of the Kohn-Sham DFT at the generalized gradient approximation (GGA) level, implemented in the Vienna *ab initio* simulation package (VASP).[56–60] The GGA was formulated by the Perdew-Burke-Ernzerhof density functional.[61,62] The Gaussian broadening technique was adopted. All calculations presented in this study were performed with one unit cell comprising 176 and 184 atoms for $\square V_2Al_{20}$ and AV_2Al_{20}, respectively. A k–mesh of 7x7x7 points in the Monkhorst–pack scheme and the energy cut–off of 375 eV were applied.

A series of energy minimization runs for a variation of the cell volume up to ±5 % were carried out to compute the equation of state (EoS) of the compounds. Bulk moduli $B_\circ$, their pressure derivatives B' and equilibrium volumes $V_\circ$ were derived from a match of the Birch–Murnaghan equation

$$\begin{aligned} U(V) = U_\circ + \frac{9B_\circ V_\circ}{16}[(V/V_\circ)^{\frac{2}{3}} - 1]^2 \\ [6 + B'(V/V_\circ)^{\frac{2}{3}} - 1) - 4(V/V_\circ)^{\frac{2}{3}}] \end{aligned} \tag{1}$$

to the total energy data $U(V)$.[63] Atomic potentials of Al(16c) and A(8a) in $x00$ and xxx directions were examined by displacing the respective atoms, one at a time, with a gradually increasing amplitude up to the maximum of $\Delta x \pm 0.55$ Å. $x00$ and xxx correspond to the directions of the displacements exploited for the computation of Hellmann–Feynman forces and to the direct view between the 16c and 8a sites, respectively. The applied mesh of displacements can be concluded upon from figures reported hereafter.

The vibrational dynamics of the compounds were calculated by the direct method implemented in the program PHONON based on Hellmann–Feynman forces derived from a series of single point energy calculations.[64,65] A Q–mesh of $2 \cdot 10^5$ points was utilized for the calculation of the total $Z(\omega)$ and partial $Z_\mathrm{n}(\omega)$ vibrational densities of states with n denoting the constituents of the compounds. Corresponding response functions such as the thermal displacement parameters $U^\mathrm{n}_\mathrm{iso}(T)$,

$$U^\mathrm{n}_\mathrm{iso}(T) = \frac{1}{2}\frac{\hbar}{M_\mathrm{n}}\int \frac{Z_\mathrm{n}(\omega)}{\omega}\coth\left(\frac{\hbar\omega}{2k_\mathrm{B}T}\right)\mathrm{d}\omega \quad , \tag{2}$$

and heat capacities

$$C_V(T) = k_\mathrm{B}\int\left(\frac{\hbar\omega}{k_\mathrm{B}T}\right)^2 \frac{Z(\omega)}{\sinh^2\left(\frac{\hbar\omega}{2k_\mathrm{B}T}\right)}\mathrm{d}\omega \quad , \tag{3}$$

were computed within the harmonic approximation. M_n represents the elemental mass, k_B the Boltzmann, and $\hbar$ the Planck constants.

Anharmonicity effects were examined from Hellmann–Feynman forces computed with structures whose lattice parameters were varied by ±1 ‰ from the equilibrium values. Mode Grüneisen parameters

$$\gamma(\omega_\mathrm{i}) = -\frac{\Delta\ln\omega_\mathrm{i}}{\Delta\ln V} \quad , \tag{4}$$

the associated thermodynamic Grüneisen parameters

$$\Gamma(T) = \frac{\sum_{\mathrm{i}} \gamma(\omega_{\mathrm{i}}) C_{\mathrm{i}}(T)}{\sum_{\mathrm{i}} C_{\mathrm{i}}(T)} \quad , \tag{5}$$

and the coefficient of linear thermal expansion

$$\alpha(T) = \frac{\sum_{\mathrm{i}} \gamma(\omega_{\mathrm{i}}) C_{\mathrm{i}}(T)}{3 V_{\circ} B_{\circ}} \quad , \tag{6}$$

were computed. The mode specific heat at constant V is

$$C_{\mathrm{i}}(T) = k_{\mathrm{B}} \left(\frac{\hbar \omega_{\mathrm{i}}^{\circ}}{k_{\mathrm{B}} T} \right)^2 \frac{\exp\left(\frac{\hbar \omega_{\mathrm{i}}^{\circ}}{k_{\mathrm{B}} T}\right)}{\left[\exp\left(\frac{\hbar \omega_{\mathrm{i}}^{\circ}}{k_{\mathrm{B}} T}\right) - 1\right]^2} \quad . \tag{7}$$

We limited this consideration to modes at the Brillouin–zone center (Γ point). Consequently, $\omega_{\mathrm{i}}^{\circ}$ denotes the ground state Γ–point energies and the summation is carried out over all Γ–point modes i.

To allow a direct comparison of the computer generated response with experimental data we applied the PALD technique to compute the Q–resolved and orientationally averaged phonon form–factors of the compounds.[33,36,39,40] A total of 10^5 Q–points in the wave vector range 0–10 Å^{-1} was exploited for the PALD response. Extracting the phase–space region monitored by the IN6@ILL and IN4@ILL instruments, accounting for the scattering lengths and cross sections of the compounds' constituents, and approximating the energy resolution of the spectrometers allows to compute a PALD–generated Q–averaged generalized density of states $G'(\omega)$ in analogy to the measured $G(\omega)$. To highlight the strong differences in the scattering properties of the compounds' constituents we report in table I their scattering powers. Note for example that the probability of scattering neutrons from scandium is almost one order of magnitude higher than the scattering probability from aluminum, hence, leading to an enhanced departure of the measured spectral density $G(\omega)$ from the phonon density of states $Z(\omega)$.

III. RESULTS

A. Equation of State and Structural Properties

Figure 3 depicts the EoS data and the resulting lattice parameters in comparison to the x–ray powder and single–crystal diffraction results and to literature data. Parameters obtained from the fits with eq. 1 are listed in table II. Table III offers a comparison of the fractional coordinates x, y, z obtained for the DFT optimized structures and derived from the x–ray diffraction experiments.

We note a good match of the DFT results with the experimental data. In particular, the changes of the lattice parameter a upon the variation of the cation A are reproduced successfully. Note that for the comparison of the DFT derived $\square V_2Al_{20}$ with literature data results on weakly doped ternary compounds have been chosen, such as $Ga_{0.05}V_2Al_{20}$ with 14.51179(1) Å from Ref. 22 and $Al_{0.3}V_2Al_{20}$ with 14.5157(8) Å from Ref. 24.

There is a small however clear departure of the DFT data towards smaller values when compared with measured a. Its extent can be attributed to the thermal expansion of the compounds, as all experimental results referred to here have been obtained at room temperature in contrast to the zero–point ground–state DFT calculations. Kontio et al. establish in Ref. 66 an increase of a by about 0.03 Å between 100 and 295 K for $Al_{0.85}V_2Al_{20}$. For $Al_{0.2}V_2Al_{20}$ we estimate an increase by about 0.05 Å between 0 and 200 K from linear expansion data of Safarik et al. 23.

A close match is observed to DFT results of Jahnatek et al. reporting $a = 14.460$ Å in Ref. 67 and Wang et al. reporting $a = 14.449$ Å in Ref. 68. An equally good match is found for the bulk moduli with $B = 85$ GPa and $B_0 = 86.1$ GPa determined by Jahnatek et al. and Wang et al., respectively. Safarik et al. establish $B_{\mathrm{T,S}}(T = 0) \approx 87.7$ GPa for $Al_{0.2}V_2Al_{20}$ in experiments.[23]

B. Lattice Dynamics Calculations

Computed Γ–point frequencies are listed in table IV. They correspond to $\omega_{\mathrm{i}}^{\circ}$ exploited in eq. 7. Phonon dispersions $\hbar\omega(\mathbf{Q})$ along high–symmetry directions are reported in Fig. 4. For clarity we restrict the presentation of the phonon eigenmodes to the low–energy region only. At higher energies the density of eigenmodes is too high to allow significant conclusions upon differences in $\hbar\omega(\mathbf{Q})$ between the different compounds. A more apprehensible information is hence offered by the total $Z(\omega)$ and partial vibrational densities of states $Z_{\mathrm{n}}(\omega)$. They are reported in Fig. 5.

Depending on the occupation of the 8a site significant changes in the total $Z(\omega)$ are observable at $\hbar\omega \lesssim 20$ meV ($\lesssim 5$ THz). At $\hbar\omega > 20$ meV only a subtle renormalization of the response can be identified. As expected, at $\hbar\omega \lesssim 20$ meV the cation vibrations dominate the inelastic response. Their coupling to each of the unique atoms is significantly different with the strongest effect on the Al(16c) dynamics. Al(16c) exhibits a localized density of states peaking at around 16 meV in the binary compound. In ScV_2Al_{20} the localized $Z_{Al(16c)}(\omega)$ splits into two bands with characteristic energies of about 16 meV and 24 meV. These bands are renormalized to 12 and 30 meV in LaV_2Al_{20} and to 15 and 28.5 meV in CeV_2Al_{20}. As can be seen from the texture of the partial densities of states, the renormalization of the low–energy maximum is due to a strong hybridization with the A(8a) vibrations. To quantify these findings the mean energies $\overline{E}_\mathrm{n}$ and the variances $\widetilde{E}_\mathrm{n}$ of A(8a) and Al(16c) were calculated as

$$\overline{E}_\mathrm{n} = \int \hbar\omega Z_\mathrm{n}(\omega)\mathrm{d}\omega \quad ,$$

$$\widetilde{E}_\mathrm{n} = \int (\hbar\omega)^2 Z_\mathrm{n}(\omega)\mathrm{d}\omega - \overline{E}_\mathrm{n}^2 \quad .$$

They are listed in table V. Averaged velocities of sound v_av and Debye temperatures Θ_D calculated from the Debye–level of $\lim_{\omega\to 0} Z(\omega)/\omega^2$ are as well listed.

A concomitant hybridization of A(8a) vibrations is formed with the Al(48f) and Al(96g) dynamics leading to a mode deficiency around 17 meV in LaV_2Al_{20} and CeV_2Al_{20}. This effect is as well visualized by their phonon dispersions in Fig. 4 through a concentration of localized eigenmodes at 2.7–3.5 THz (11.2–14.5 meV) in LaV_2Al_{20}, and at 2.8–3.8 THz (11.6–15.7 meV) in CeV_2Al_{20}. Effectively and unlike $Z_\mathrm{Al(16c)}(\omega)$, $Z_\mathrm{Al(48f)}(\omega)$ and $Z_\mathrm{Al(96g)}(\omega)$ are distributed over the entire range of eigenmodes. In accordance with $Z(\omega)$ they exhibit only a weak renormalization at $\hbar\omega > 20$ meV for different occupants of the 8a sites. The dynamics of vanadium (16d) is in line with these results. However, for $\hbar\omega \lesssim 20$ meV its density of states is characterized by a low, flat and textureless profile.

The most distinct influence on the collective vibrations is generated by the inclusion of Sc. In ScV_2Al_{20} its characteristic frequencies are located below the first optic modes of the binary compound. These optic modes are dominated by Al(96g) vibrations and can be identified from the first strong peak at about 11.6 meV (2.8 THz) in the densities of states in Fig. 5 as well as by the flat phonon dispersions at this energy in Fig. 4. Thus, Sc hybridizes weakly with the V_2Al_{20} vibrations forming the additional dispersionless optic phonons at energies down to 5 meV (1.2 THz). Small peaks in $Z_\mathrm{Al(16c)}(\omega)$ and $Z_\mathrm{Al(96g)}(\omega)$ matching the texture of $Z_\mathrm{Sc(8a)}(\omega)$ give evidence of this weak hybridization.

We indicate by the red dashed line drawn with the phonon dispersion of ScV_2Al_{20} in Fig. 4 the boundary below which the Sc generated optic phonons dominate the collective dynamics. Unlike in $\square V_2Al_{20}$, LaV_2Al_{20}, and CeV_2Al_{20} in which the Γ–point modes of lowest energy are optically silent (T2u, A2g symmetries) as indicated in table IV, in ScV_2Al_{20} they are infra–red (T1u) and Raman (T2g) active eigenstates.

C. Atomic Potentials and Force Constants

Some features of the established collective dynamics can be broken down to the shape of atomic potentials approximated on the DFT level and to force constants determining the LDC. Atomic potentials $U(\Delta x)$ of Al(16c) and A(8a) are reported in Fig. 6. Table VI reports parameters obtained from approximating the potentials as $U(\Delta x) = A\Delta x^2 + B\Delta x^4$ within the extensive displacement range of $[-0.25, 0.25]$ Å.

The occupation of the 8a site by the different cations has two effects on the harmonic part (A parameters) of the Al(16c) potentials. Firstly, the restoring forces are gradually augmented in both monitored directions in the sequence of Sc, Ce and La occupants. Thereby A^{Al}_{xxx} is approximately tripled in LaV_2Al_{20} and CeV_2Al_{20} . A^{Al}_{x00} is increased by about 50 % only. Secondly, a moderate anisotropy present in $\square V_2Al_{20}$ with $A^{\mathrm{Al}}_{x00} \gtrsim A^{\mathrm{Al}}_{xxx}$ is enhanced simultaneously. It takes on the highest value in LaV_2Al_{20} whereby $A^{\mathrm{Al}}_{x00} \ll A^{\mathrm{Al}}_{xxx}$. This anisotropy and its systematic variation are the origin of the formation and shifting of the two maxima in $Z_{\mathrm{Al(16c)}}(\omega)$ shown in Fig. 5.

In contrast to the Al(16c) potentials, the harmonic contribution to $U(\Delta x)$ of A(8a) is isotropic. A^{M}_{x00} and A^{M}_{xxx} do not change systematically with A^{Al}_{x00} and A^{Al}_{xxx} in the respective compounds but take on a minimum for Sc and a six times higher maximum for La. Since the mass ratio of La and Ce with Sc corresponds only to about three (see table I) the characteristic frequency of the heavy cations La and Ce is to be expected at higher values as evidenced by the $Z_{A\mathrm{(8a)}}(\omega)$ in Fig. 5.

In the binary compound the potential of Al(16c) appears to be considerably anharmonic in $x00$ direction. This anharmonicity is progressively suppressed in the ternary compounds following the sequence of Sc, Ce and La occupants. On the other hand the potential appears to be perfectly harmonic in xxx direction with $B^{\mathrm{Al}}_{xxx} = 0$.

However, the most striking result of the potential analysis is the distinctive anharmonicity of Sc. As can be seen in Fig. 6 the $U(\Delta x)$ of Sc is strongly reminiscent of a flat bottom potential. Note that the quality of the match of the quartic analytical function does not depend significantly on the fitting range, as we have probed in different fitting approaches not discussed here. Clearly, the quartic term is found to be intrinsic to the DFT–computed Sc potential. Terms of higher order such as of sextic proved to be redundant. Apart from its indispensable significance for the modelling of the Sc potential the quartic term proved to be of relevance to improve the fit quality for Al(16c) in $\square V_2Al_{20}$ along $x00$.

The parameters A should reflect the harmonic forces derived from the Hellmann–Feynman forces through the LDC. The nonzero components of the 3×3 force matrix F_{ij} are listed in Table VII. They match the expected relations of $2A_{x00} = F_{\mathrm{ii}}$ and $2A_{xxx} = F_{\mathrm{ii}} + 2F_{\mathrm{ij}}$ with $\mathrm{i, j = x, y, z}$ and prove the consistence of the potential analysis.

D. Inelastic Neutron Scattering and Powder Average Lattice Dynamics

Figure 7 depicts the phonon formfactor of ScV_2Al_{20} at $T = 300$ K and the corresponding relative Debye–Waller factor (DWF) computed by PALD. The effect of the elevated temperature is visualized by the decrease of the DWF towards high wave vectors Q. This decrease is particularly pronounced for vibrational modes to which Sc contributes with high amplitudes, i.e. to modes at $4 \lesssim \hbar\omega \lesssim 10$ meV. In INS experiments the phonon intensity is determined by $F(\mathbf{Q}, \omega, T)$ comprising the DWF.[40] Thence, the characteristics of the Sc dynamics are detectable at low Q only evidenced by the pronounced signal localized at $1 \lesssim Q \lesssim 5$ Å^{-1} and $4 \lesssim \hbar\omega \lesssim 10$ meV in $F(\mathbf{Q}, \omega, T = 300\text{ K})$ in Fig. 7.

Figure 8 reports the generalized densities of states $G(\omega)$ derived from INS experiments at IN6@ILL and from according PALD calculations $G'(\omega)$. The phase space covered by the experiment as well as exploited for the PALD is sketched in Fig.7. The scatter towards high energies of the experimental data taken at 100 K results from reduced intensity due to the lowered Bose–Einstein occupation number. Note that at 100 K a peak around 22 meV becomes detectable stemming from elastic second–order scattering of the spectrometer's monochromator.

We find an overall good match between the experimental and PALD data sets. In any of the measured $G(\omega)$ pronounced low–energy peaks are identified giving evidence of the localization of the Sc, La and Ce dominated vibrations at low energies as discussed above.

In particular for LaV_2Al_{20} and CeV_2Al_{20} the overall spectral distribution, the characteristic peaks and their relative intensities are well reproduced by the PALD. Note that the distinguished maximum at about 30 meV present only in $G(\omega)$ of LaV_2Al_{20} and CeV_2Al_{20} corresponds to the characteristic maximum in $Z_{\mathrm{Al(16c)}}(\omega)$ in these compounds.

Despite the overall good approximation of the ScV_2Al_{20} INS response the match is less satisfactory for two reasons. Firstly, the pronounced low–energy peak dominated by Sc dynamics is shifted towards low energies in the PALD data. Although, the experimental results give evidence of a positive anharmonicity $\mathrm{d}\omega(T)/\mathrm{d}T > 0$ of this peak between 100 and 300 K, this anharmonicity is too small to compensate for the overall mismatch of this peak even at base temperature. Secondly, the spectral shape of the PALD distribution indicates better resolved peaks than found in the experimental $G(\omega)$. Obviously the analytically approximated energy–dependent resolution function of the spectrometer, which has been convoluted with the PALD results, is not fully sufficient to account for the broadening of peaks in the experimental signal of ScV_2Al_{20}.

To shed more light on the anharmonicity of the Sc–, La– and Ce–dominated low–energy modes and their spectral distribution Fig. 9 reports the Q–averaged dynamic structure factors $S(\omega, T)$ derived from IN4@ILL experiments. $S(\omega, T)$ has been corrected for the Bose–Einstein occupation number, thence, the intensity changes reflect the T dependence of the DWF only.

The INS derived $S(\omega, T)$ are affected by following experimental effects. Bragg reflections are mediated through the energy resolution of the spectrometer and disguise the inelastic signal at $\hbar\omega \rightarrow 0$ for $T \rightarrow 0$ as evidenced in Fig. 9. In general, lattice dynamics calculations do not account for elastic signals. Moreover, the compounds incoherent scattering mainly given by vanadium (see table I) contributes to the INS response. It is not accounted for by our PALD approach as it contributes monotonically as a flat background to the signal in the energy ranges considered in Fig. 9.

Aside from these effects, the PALD approach reproduces the properties of the low–energy modes with high quality. For LaV_2Al_{20} and CeV_2Al_{20} the spectral shape and its T response are captured in detail. Weak anharmonicity is revealed by the experiment evidenced by a smearing and a weak red–shift $\mathrm{d}\omega(T)/\mathrm{d}T < 0$ of peaks upon heating. Within the quality of the present data we quantify this shift to about -0.2(1) meV between 2 and 300 K. However, this shift does not apply universally to all identified peaks. We highlight only the behaviour of the small peak at about 14.5 meV in $\mathrm{LaV_2Al_{20}}$ response whose T shift is roughly doubled. According to $Z_\mathrm{n}(\omega)$ it is dominated by Al(96g) vibrations. A similar conclusion can be drawn for the peak around 12 meV in $\mathrm{CeV_2Al_{20}}$.

For $\mathrm{ScV_2Al_{20}}$ the IN4@ill data firm up the observations made with the IN6@ILL measurements. As expected from the PALD calculations the intensity loss due to the T–dependence of the DWF is strongest for $\mathrm{ScV_2Al_{20}}$, in spite of the smaller Q range monitored. In comparison to the PALD results the Sc–dominated modes are localized at higher energies and specific peaks, although implied in the low–energy maximum, barely resolved. Upon increasing T this maximum exhibits a pronounced blue–shift $\mathrm{d}\omega(T)/\mathrm{d}T > 0$ in contrast to the $\mathrm{LaV_2Al_{20}}$ and $\mathrm{CeV_2Al_{20}}$ response.

To quantify the anharmonic response of $\mathrm{ScV_2Al_{20}}$ the low–energy part of $G(\omega)$ has been matched by a set of Gaussians and a Debye ω^2 contribution. Two Gaussians are sufficient to approximate the IN4@ILL results, whereby the anti–Stokes line which is not shown here has been exploited separately down to 50 K. IN6@ILL results have been approximated by three Gaussians one explicitely dedicated to match a peak around 11.5 meV. This peak is identified by lattice dynamics calculation in Fig. 5 being dominated by Al(96g) 8dynamics and marked by the red dotted line in Fig. 8. Results are displayed in Fig. 10.

We report the energy positions of the peaks with the Stokes–line data explicitely discriminated as $E_1(T)$ and $E_2(T)$ as well as the moments of energy $\langle E(T)\rangle$ computed from the 2– and 3–Gaussian spectra, respectively. The entire set of $\langle E(T)\rangle$ has been matched by a linear T–dependence $E(T) = E^* + C \cdot T$ with $E^* = 7.745$ meV and $C = 0.007379$ meV/K as indicated by the solid line in Fig. 10. To classify the strength of the anharmonicity we interprete the values of $E_1(T)$, $E_2(T)$ and $\langle E(T)\rangle$ in terms of the Dahm and Ueda model (DUM) introduced in Ref. 69. As indicated by the gray shaded area in Fig. 10 the evolution of the entire set of data is in agreement with an anharmonicity parameter β in the range of 0.15–0.5.

The T–variation of the low–energy modes in $\mathrm{ScV_2Al_{20}}$ evidences the presence of a term surmounting the cubic term characteristic of thermal expansion.[41] It is thus in agreement with a strong quartic anharmonic term in the Sc potential as discussed in Sec. III C. In contrast, for La and Ce the cubic term is obviously balancing out any other contribution of higher order.

Within the single particle DUM the prefactors A and B obtained for Sc result with the free mass of Sc in the characteristic energy $E^*_{\mathrm{DUM}} \approx 11.5$ meV and the anharmonicity parameter $\beta_{DUM} \approx 0.05$. These values are close to the characteristic energy $\overline{E}_{\mathrm{Sc}} \approx 9.0$ meV calculated from $Z_{\mathrm{Sc}}(\omega)$ and to the β range estimated from experimental data. The correspondance of β_{DUM} with the experimental data can be improved by taking into account the low–energy modes identified in $G(\omega)$ and thus $Z_{\mathrm{Sc}}(\omega)$ only. It is then quantified to the range of 0.15–0.2.

E. Thermal Displacement Parameters

Figure 11 depicts the element specific thermal displacement parameters $U^{\mathrm{n}}_{\mathrm{iso}}(T)$ derived from the partial phonon densities of states $Z_n(\omega)$ through eq. 2. Note, that $U^{\mathrm{Al}}_{\mathrm{iso}}(T)$ and $U^{\mathrm{V}}_{\mathrm{iso}}(T)$ of the $\square V_2Al_{20}$ compound are not explicitely displayed as they are very similar to and well represented by the corresponding values determined for ScV_2Al_{20}.

We exploited in addition the experimentally determined energy shift $E(T)$ shown in Fig. 10 to reconstruct an effective $Z[\omega(T)]$ which respects the renormalization of the low–energy modes in ScV_2Al_{20}. Thereby, an effective $Z_{\mathrm{Sc}}[\omega(T=0)]$ was generated to which only the localized signal between 4.9 and 10.4 meV in $Z_{\mathrm{Sc}}(\omega)$ was assigned to. $\Delta\hbar\omega(T) = CT$ with $C = 0.007379$ meV/K. The weakly textured signal at $\hbar\omega \leq 10.4$ meV in $Z_{\mathrm{Al}}(\omega) + Z_{\mathrm{V}}(\omega)$ was replaced by a Debye–like $\propto \omega^2$ signal respecting Θ_{D} listed in table V Finally, $Z[\omega(T)]$ was reconstructed from both contributions respecting their expected relative number of vibrational modes.

In the present x–ray diffraction experiments on powder materials the partial occupancies and site disorder in the AV_2Al_{20} compounds as well as the low contrast of aluminum lead to high uncertainties and $U^{\mathrm{n}}_{\mathrm{iso}}(T)$ values. They are one order of magnitude higher than values obtained with single crystals and for this reasons not discussed here. The single crystal data shown in Fig. 11, however, match reasonably well the DFT results and trends in the atomic displacements. Taking as well into consideration the data of Kangas et al. established in Ref. 70 and Moze et al. ($\square$) presented in Ref. 71 the $U^{\mathrm{n}}_{\mathrm{iso}}(T)$ of the different Al sites seem to scatter around the $U^{\mathrm{n}}_{\mathrm{iso}}(T)$ in a way as to balance out each other for an overall reasonable fit.

Data on $Al_{0.2}V_2Al_{20}$ from neutron diffraction experiments by Safarik et al. discussed in Ref. 23 show a reasonable match with the DFT results on $\square V_2Al_{20}$. The experimentally established T–dependent deviation from a harmonic behavior of the Al(8a) displacement parameter in $Al_{0.2}V_2Al_{20}$ is qualitatively in accordance with the estimated behaviour of the $U^{\mathrm{Sc}}_{\mathrm{iso}}(T)$ in ScV_2Al_{20}.

F. Heat Capacity

Figure 12 shows the heat capacities derived from $Z(\omega)$ through eq. 3. The right subfigure focuses on the low T region and highlight the excess of vibrational modes on the heat capacity of ScV_2Al_{20} in equivalence to the properties of Al and Ga containing compounds.[22–24] The difference between the $C_V(T)$ of ScV_2Al_{20} and LaV_2Al_{20} indicates by its negative values from about 80 K on that the cummulative number of vibrational modes in LaV_2Al_{20} is higher when integrated up to 12–18 meV.

With the DFT derived data we report as well the effect of the phonon renormalization on $C_V(T)/T$ data of ScV_2Al_{20} calculated with $Z[\omega(T)]$. Despite a visible acces of intensity at low T in ScV_2Al_{20} their $C_V(T)/T$ does not display a pronounced shoulder as evidenced in Ga and Al containing V_2Al_{20}.[4,22–24] This can be expected as the characteristic modes of Sc are located at higher energies than those of Ga and Al, and, moreover, the energy shift upon T–variation of Al–dominated vibrations is supposed to be enhanced.[4] The variation brought about by $Z[\omega(T)]$ is rather subtle. It is detectable as a dilution of the difference amplitude in respect to LaV_2Al_{20} albeit a higher signal towards low T is present.

G. Grüneisen Parameters and Thermal Expansion

Figure 13 shows the mode Grüneisen parameter $\gamma(\omega_{\mathrm{i}})$, the thermodynamic Grüneisenparameter $\Gamma(T)$ and the coefficient of linear thermal expansion $\alpha(T)$ calculated through eqs. 4, 5, and 6. In full accordance to the reconstruction of an effective $Z[\omega(T)]$ of ScV_2Al_{20} we carried out a renormalization of the two low–energy Γ–point frequencies. The corresponding $\Gamma(T)$ and $\alpha(T)$ are as well displayed in Fig. 13.

The properties of $\gamma(\omega_{\mathrm{i}})$ are correlated with the partial contributions of the elements to the eigenmodes. Vibrations at energies above 20 meV which are dominated by the amplitudes of Al(48f), Al(96g) and V tend to take on $\gamma(\omega_{\mathrm{i}})$ values between 1.5 and 2.0. In the energy range of strong Al(16c) participation $\gamma(\omega_{\mathrm{i}})$ rise to about 3 as can be specifically seen with the modes between 16 and 18 meV in $\square V_2Al_{20}$ as well as below 15 meV in LaV_2Al_{20}. Whereas in LaV_2Al_{20} the effect of the A(8a) contribution on $\gamma(\omega_\mathrm{i})$ is moderate due to the strong hybridization with the lattice modes in ScV_2Al_{20} values of about 12 are derived for the two low–energy modes.

As an effect of the pristine LDC results the enhanced anharmonicity in ScV_2Al_{20} raises visibly $\Gamma(T)$ and $\alpha(T)$ above the ones of $\Box V_2Al_{20}$ and LaV_2Al_{20}. High–T values of $\Gamma(T)$ correspond to 1.7, 2.3 and 1.8 for $\Box V_2Al_{20}$, ScV_2Al_{20} and LaV_2Al_{20}, respectively. The relative behaviour of $\alpha(T)$ at elevated T follows accordingly. At low–T the deviation of the ScV_2Al_{20} properties is amplified as the anharmonicity is only strong for the low–energy modes.

Calculations with the renormalized low–energy modes result in high–T responses of ScV_2Al_{20} very comparable to the ones of the other compounds. $\Gamma(T)$ reaches a value of 1.8 and $\alpha(T)$ arrives close to the level of $\Box V_2Al_{20}$. Hence, properties of ScV_2Al_{20} are corrected by about 25 % by the phonon renormalization.

The overall behaviour of the LDC derived $\Gamma(T)$ and $\alpha(T)$ is in good agreement with experimental data on $Al_{0.2}V_2Al_{20}$.[23] Towards low T the $\Gamma(T)$ of $Al_{0.2}V_2Al_{20}$ shows an excess about four times stronger than in ScV_2Al_{20}. Taking into consideration the exceeding energy shift of the characteristic Al(8a) modes in $Al_xV_2Al_{20}$ this result could be conjectured.[4] To reproduce at low T a significant shoulder in $\alpha(T)$ as established by Safarik et al. for $Al_{0.2}V_2Al_{20}$ the account of stronger anharmonicity is required. Same can be stated for the slightly higher signals of $\Gamma(T)$ and $\alpha(T)$ towards high T in the experimental data, such as $\Gamma(T) \approx 2$.

IV. DISCUSSION AND CONCLUSIONS

To start with some generalities we highlight the good correspondance of the DFT and LDC results with data and conclusions drawn from computer studies on other Einstein solids such as skutterudites and clathrates published in the literature.[15,16,30,31,37,39,72] Experimentally established inelastic responses are reproduced satisfactorily with no negative eigenfrequencies indicative of instability of the computer generated compounds. The electropositive elements $A =$ Sc, La and Ce occupy center positions in the voids of the polyanionic matrix V_2Al_{20}. Low–energy excitations are identified as hybrid eigenmodes of A with V_2Al_{20} to which A contribute with higher amplitudes. As a consequence of the hybridization the eigenmodes dominated by A are distinctly dispersive leading to a number of van Hove singularities in the low–energy region of the vibrational density of states of the compounds.

From the analysis of the static, local potentials it follows that anharmonicity is enhanced for the weaker coupling and, thus, for smaller restoring forces acting on Sc. An estimation of the anharmonicity as a response to T variations by means of the DUM anharmonic model introduced in Ref. 69 indicates a positive frequency shift in the order of the detected renormalization of low–energy modes in $\mathrm{ScV_2Al_{20}}$. This shift was approximated from INS data to 2 meV upon heating the compound from 2 to 300 K which corresponds to an anharmonicity parameter $\beta = 0.15 - 0.5$ of the model. DFT derived potentials are in agreement with $\beta = 0.05 - 0.2$. Equivalent data analysis had been performed for the T response of INS data of the compounds $\mathrm{YbFe_4Sb_{12}}$ with $\beta \approx 0.014$ in Ref. 36 and $A\mathrm{Os_2O_6}$ with β ranging between 0.025 and about 1 for the different A =K, Rb, and Cs in Ref. 14. Thus, the amplitude of the phonon renormalization and the values of the β parameter in those compounds render the property of $\mathrm{ScV_2Al_{20}}$.

We exploited the positive mode shift of $\mathrm{ScV_2Al_{20}}$ to correct LDC derived data on $U^{\mathrm{Sc}}_{\mathrm{iso}}(T)$ and $C_V(T)$, as well as $\Gamma(T)$ and $\alpha(T)$ derived from volume dependent DFT calculations. The correspondance with data available in the literature on $A\mathrm{V_2Al_{20}}$ is convincing on qualitative and quantitative grounds.[4,22–25] In particular, the applied correction proves to be essential to arrive at reasonable values of $\Gamma(T)$ and $\alpha(T)$ at high temperatures and discloses thus the significance of the enhanced positive anharmonicity of the low–energy modes in $\mathrm{ScV_2Al_{20}}$. The high–T behaviour of $\Gamma(T)$ and $\alpha(T)$ show a propensity to slightly reduced values, e.g. $\alpha(T)$ is smaller by 10 % when compared with experimental results and the DFT derived pressure derivative B'. Nonetheless, it is necessary to recall that the presented thermodynamic responses were modelled with ground state parameters $V_\circ$, $B_\circ$ and ground state Γ–point distributions $\omega_{\mathrm{i}}^{\circ}$, and the applied renormalization of low–energy modes was based on the idea of a decoupled and harmonic vibrations of Sc, on one hand, and $\mathrm{V_2Al_{20}}$, on the other.

The importance of coupling and anharmonicity can be judged upon from the properties of $\mathrm{LaV_2Al_{20}}$. Unlike in $\mathrm{ScV_2Al_{20}}$ the low–energy vibrations in $\mathrm{LaV_2Al_{20}}$ show a weak softening upon heating, however, enhanced low–T $\Gamma(T)$ values and the augmented $\alpha(T)$ behaviour suggest rather a weak positive mode–shift upon heating. This apparent contrast can be explained by the thermal expansion of $\mathrm{LaV_2Al_{20}}$ balancing out the quartic term identified in the La potential as a ground–state property. The spectral densities do not shift uniformly and different peaks in $G(\omega)$ and $S(\omega, T)$ show different sensitivities upon T variations. An equivalent observation is reported in the literature for the dynamics of skutterudites and clathrates.[16,33,36,72]

There is a dynamic feature in the response of ScV_2Al_{20} which may underline coupling properties in this compound and is worth speculating about. The shift of the mean energy $\langle E(T) \rangle$ of the Sc–dominated peak does not follow strictly the prediction of the DUM but tends towards higher values at higher T as shown in Fig. 10. INS data of KOs_2O_6 show a corresponding behaviour.[14] Obviously higher restoring forces than those predicted by the static quartic potential at $T = 0$ are at work at higher T. This finding is supported by the recently discussed thermal effects of the $Al_{0.33}W_{1.67}O_6$ matrix on the effective potential of K derived through molecular dynamics simulations by Shoko et al. in Ref. 73. If it was correct, it would be in line with the conjecture of an effective sextic term dominating the thermal displacement parameter $U_{iso}^{\mathrm{Al(8a)}}(T)$ in $Al_{0.2}V_2Al_{20}$ as discussed in Ref. 23. Interestingly, we concluded as well a noticeable anharmonicity in the DFT computed Al(16c) potential akin the one communicated by Safarik et al. for $Al_{0.2}V_2Al_{20}$.

The anharmonic effects discussed so far can not explain the weak definition of peaks in the INS response of ScV_2Al_{20}. Assuming a strict correctness of our DFT and LDC results we expect characteristic peaks in ScV_2Al_{20} to be as well resolved by INS as they are in LaV_2Al_{20} and CeV_2Al_{20}. It is tempting to assign the broadening in the INS data to defects and disorder in the ScV_2Al_{20} compound. However, the validity of this assignment remains an open question here as we could not quantify a possible amount of defects in the specimen. A defective crystalline structure becomes noticeable by a reduction of its Bragg peak intensities equivalent to the impact of enhanced thermal displacements $U_{\mathrm{iso}}^{\mathrm{n}}(T)$. By the performed x–ray diffraction experiments we could not discriminate these effects. Temperature dependent neutron diffraction enhancing the contrast between Sc and Al and total scattering experiments could be of help and will be tackled in future.

Finally we highlight that the core of this study is the establishment of the microscopic dynamics of the AV_2Al_{20} with the temperature dependent effects being computed as a consequence of the ground state properties of the DFT approximated compounds. Consequently, the results do not explain the thermal conductivity data of ScV_2Al_{20} and LaV_2Al_{20} in quantitative measures as reported in Fig. 2. Nonetheless we identify two properties of the microscopic dynamics which lead to a reduced thermal conductivity in crystals and could account for the particular behaviour of $\kappa_\mathrm{l}(T)$ of $\mathrm{ScV_2Al_{20}}$ on qualitative grounds. Number one is the formation of hybrid modes of low–dispersion located within the energy range of acoustic phonons of the binary compound. Thereby, the average energy of the hybrid modes is bisected in $\mathrm{ScV_2Al_{20}}$ when compared to $\mathrm{LaV_2Al_{20}}$ disrupting propagating modes of longer wavelength and thus indicating an overall lowered $\kappa_\mathrm{l}(T)$. Number two is the enhanced mode Grüneisen parameter of the hybrid modes which is highly augmented in the Sc containing compound facilitating shorter phonon lifetimes and leading to lowered $\kappa_\mathrm{l}(T)$. With increasing T the low–energy hybrid modes of $\mathrm{ScV_2Al_{20}}$ are renormalized approaching energies of the $\mathrm{LaV_2Al_{20}}$ hybrid modes thence being indicative of a progressive reduction of the difference in $\kappa_\mathrm{l}(T)$ between these two compounds. In summary, the measured $\kappa_\mathrm{l}(T)$ plotted in Fig. 2 is qualitatively in line with the properties of the microscopic dynamics established experimentally by INS and through DFT and LDC.

V. SUMMARY

We have shown that the microscopic dynamics of $A\mathrm{V_2Al_{20}}$ (A = Sc, La, and Ce) which was monitored by inelastic neutron scattering experiments can be approximated by a set of vibrational eigenmodes derived through density finctional theory (DFT) and lattice dynamics calculations (LDC). Structural properties studied experimentally have been equally matched on qualitative and quantitative grounds by the computer modelling. The propensity of the DFT–derived potential of A(8a) and Al(16c) sites to anharmonicity with a significant quartic term has been established and experimentally confirmed in $\mathrm{ScV_2Al_{20}}$ by a positive renormalization of Sc–dominated modes upon heating in INS experiments. It has been demonstrated for $\mathrm{ScV_2Al_{20}}$ that with the aid of DFT and LDC–derived mode Grüneisen parameters and the experimentally deduced mode shift an optimization of the characterization of thermal displacements, specific heats, thermodynamic Grüneisen parameters and thermal expansions can be performed.

---

[1] B. C. Sales, *Handbook on the Physics and Chemistry of the Rare Earths* (2002).

[2] G. S. Nolas, D. T. Morelli, and T. M. Tritt, Annu. Rev. Mater. Sci. **29**, 89 (1999).

[3] G. S. Nolas, J. Sharp, and H. J. Goldsmid, *Thermoelectrics Basic Principles and New Materials Developments* (Springer, 2001).

[4] A. D. Caplin and L. K. Nicholson, Journal of Physics F: Metal Physics **8**, 51 (1978), URL `http://stacks.iop.org/0305-4608/8/i=1/a=010`.

[5] V. Keppens, D. Mandrus, B. C. Sales, B. C. Chakoumakos, P. Dai, R. Coldea, M. B. Maple, D. A. Gajewski, E. J. Freeman, and S. Bennington, Nature **395**, 876 (1998).

[6] R. P. Hermann, R. Jin, W. Schweika, F. Grandjean, D. Mandrus, B. C. Sales, and G. J. Long, Phys. Rev. Lett. **90**, 135505 (2003).

[7] R. Viennois, L. Girard, D. Ravot, H. Mutka, M. Koza, F. Terki, S. Charar, and J.-C. Tedenac, Physica B **350**, e403 (2004).

[8] R. Viennois, L. Girard, M. M. Koza, H. Mutka, D. Ravot, F. Terki, S. Charar, and J.-C. Tedenac, Phys. Chem. Chem. Phys. **7**, 1617 (2005).

[9] M. Christensen, F. Juranyi, and B. B. Iversen, Physica B: Condensed Matter **385386, Part 1**, 505 (2006), ISSN 0921-4526, proceedings of the Eighth International Conference on Neutron Scattering, URL `http://www.sciencedirect.com/science/article/pii/S092145260601132X`.

[10] R. Viennois, P. Toulemonde, M. Koza, H. Mutka, A. S. Miguel, and R. Lortz, Journal of Physics: Conference Series **92**, 012121 (2007), URL `http://stacks.iop.org/1742-6596/92/i=1/a=012121`.

[11] N. Melnychenko-Koblyuk, A. Grytsiv, L. Fornasari, H. Kaldarar, H. Michor, F. Rhrbacher, M. Koza, E. Royanian, E. Bauer, P. Rogl, et al., Journal of Physics: Condensed Matter **19**, 216223 (2007), URL `http://stacks.iop.org/0953-8984/19/i=21/a=216223`.

[12] N. Melnychenko-Koblyuk, A. Grytsiv, P. Rogl, M. Rotter, E. Bauer, G. Durand, H. Kaldarar, R. Lackner, H. Michor, E. Royanian, et al., Phys. Rev. B **76**, 144118 (2007), URL `http://link.aps.org/doi/10.1103/PhysRevB.76.144118`.

[13] R. Lortz, R. Viennois, A. Petrovic, Y. Wang, P. Toulemonde, C. Meingast, M. M. Koza, H. Mutka, A. Bossak, and A. S. Miguel, Phys. Rev. B **77**, 224507 (2008), URL `http://link.aps.org/doi/10.1103/PhysRevB.77.224507`.

[14] H. Mutka, M. M. Koza, M. R. Johnson, Z. Hiroi, J.-I. Yamaura, and Y. Nagao, Phys. Rev. B **78**, 104307 (2008).

[15] M. M. Koza, L. Capogna, A. Leithe-Jasper, H. Rosner, W. Schnelle, H. Mutka, M. R. Johnson, C. Ritter, and Y. Grin, Phys. Rev. B **81**, 174302 (2010).

[16] M. M. Koza, M. R. Johnson, H. Mutka, M. Rotter, N. Nasir, A. Grytsiv, and P. Rogl, Phys. Rev. B **82**, 214301 (2010), URL `http://link.aps.org/doi/10.1103/PhysRevB.82.214301`.

[17] M. Christensen, S. Johnsen, and B. B. Iversen, Dalton Trans. **39**, 978 (2010).

[18] A. D. Caplin, G. Grüner, and J. B. Dunlop, Phys. Rev. Lett. **30**, 1138 (1973), URL `http://link.aps.org/doi/10.1103/PhysRevLett.30.1138`.

[19] K. Iwasa, M. Kohgi, H. Sugawara, and H. Sato, Physica B **378–380**, 194 (2006).

[20] C. Lee, I. Hase, H. Sugawara, H. Yoshizawa, and H. Sato, J. Phys. Soc. Jpn. **75**, 123602 (2006).

[21] Z. Hiroi, J.-I. Yamaura, and K. Hattori, Journal of the Physical Society of Japan **81**, 011012 (2012), http://journals.jps.jp/doi/pdf/10.1143/JPSJ.81.011012, URL `http://journals.jps.jp/doi/abs/10.1143/JPSJ.81.011012`.

[22] Z. Hiroi, A. Onosaka, Y. Okamoto, J.-i. Yamaura, and H. Harima, Journal of the Phyical Society of Japan **81**, 124707 (2012).

[23] D. J. Safarik, T. Klimczuk, A. Llobet, D. D. Byler, J. C. Lashley, J. R. O'Brien, and N. R. Dilley, Phys. Rev. B **85**, 014103 (2012), URL `http://link.aps.org/doi/10.1103/PhysRevB.85.014103`.

[24] A. Onosaka, Y. Okamoto, J.-i. Yamaura, and Z. Hiroi, Journal of the Phyical Society of Japan **81**, 023703 (2012).

[25] A. Onosaka, Y. Okamoto, J.-i. Yamaura, T. Hirose, and Z. Hiroi, Journal of the Phyical Society of Japan **81**, 123702 (2012).

[26] T. Isono, D. Iguchi, T. Matsubara, Y. Machida, B. Salce, J. Flouquet, H. Ogusu, J.-i. Yamaura, Z. Hiroi, and K. Izawa, Journal of the Physical Society of Japan **82**, 114708 (2013), http://journals.jps.jp/doi/pdf/10.7566/JPSJ.82.114708, URL `http://journals.jps.jp/doi/abs/10.7566/JPSJ.82.114708`.

[27] N. Bernstein, J. L. Feldman, and D. J. Singh, Phys. Rev. B **81**, 134301 (2010).

[28] B. Huang and M. Kaviany, Acta Materialia **58**, 4516 (2010).

[29] E. S. Toberer, A. Zevalkink, and G. J. Snyder, J. Mater. Chem. **21**, 15843 (2011), URL `http://dx.doi.org/10.1039/C1JM11754H`.

[30] J. L. Feldman, P. Dai, T. Enck, B. C. Sales, D. Mandrus, and D. J. Singh, Phys. Rev. B **73**, 014306 (2006).

[31] P. Ghosez and M. Veithen, J. Phys.: Condens. Matter **19**, 096002 (2007).

[32] S. Tsutsui, H. Kobayashi, D. Ishikawa, J. P. Sutter, A. Q. R. Baron, T. Hasegawa, N. Ogita, M. Udagawa, Y. Yoda, H. Onodera, et al., J. Phys. Soc. Jpn. **77**, 033601 (2008).

[33] M. M. Koza, M. R. Johnson, R. Viennois, H. Mutka, L. Girard, and D. Ravot, Nature Mater. **7**, 805 (2008).

[34] M. Christensen, A. B. Abrahamsen, N. B. Christensen, F. Juranyi, N. H. Andersen, K. Lefmann, J. Andreasson, C. R. H. Bahl, and B. B. Iversen, Nature Mater. **7**, 811 (2008).

[35] D. Wee, B. Kozinsky, N. Marzari, and M. Fornari, Phys. Rev. B **81**, 045204 (2010).

[36] M. M. Koza, A. Leithe-Jasper, H. Rosner, W. Schnelle, H. Mutka, M. R. Johnson, M. Krisch, L. Capogna, and Y. Grin, Phys. Rev. B **84**, 014306 (2011).

[37] H. Euchner, S. Pailhès, L. T. K. Nguyen, W. Assmus, F. Ritter, A. Haghighirad, Y. Grin, S. Paschen, and M. de Boissieu, Phys. Rev. B **86**, 224303 (2012), URL `http://link.aps.org/doi/10.1103/PhysRevB.86.224303`.

[38] S. Tsutsui, H. Uchiyama, J. P. Sutter, A. Q. R. Baron, M. Mizumaki, N. Kawamura, T. Uruga, H. Sugawara, J.-i. Yamaura, A. Ochiai, et al., Phys. Rev. B **86**, 195115 (2012), URL `http://link.aps.org/doi/10.1103/PhysRevB.86.195115`.

[39] M. Marek Koza, D. Adroja, N. Takeda, Z. Henkie, and T. Cichorek, Journal of the Physical Society of Japan **82**, 114607 (2013), http://journals.jps.jp/doi/pdf/10.7566/JPSJ.82.114607, URL `http://journals.jps.jp/doi/abs/10.7566/JPSJ.82.114607`.

[40] M. M. Koza, A. Leithe-Jasper, H. Rosner, W. Schnelle, H. Mutka, M. R. Johnson, and Y. Grin, Phys. Rev. B **89**, 014302 (2014), URL `http://link.aps.org/doi/10.1103/PhysRevB.89.014302`.

[41] N. Ashcroft and N. Mermin, *Solid State Physics* (Saunders College Philadelphia, USA, 1976).

[42] S. R. Elliott, *The Physics and Chemistry of Solids* (John Wiley and Sons, 1998), ISBN 047198194x; 0471981958.

[43] G. Squires, *Introduction to the Theory of Thermal Neutron Scattering* (Dover Publications, Inc., Mineola, New York, 1996).

[44] S. Lovesey, *Theory of Neutron Scattering from Condensed Matter* (Oxford Science Publications, Oxford, UK, 1984).

[45] B. C. Sales, B. C. Chakoumakos, B. Mandrus, and J. W. Sharp, Journal of Solid State Chemistry **146**, 528 (1999).

[46] W. Schnelle, A. Leithe-Jasper, H. Rosner, R. Cardoso-Gil, R. Gumeniuk, D. Trots, J. A. Mydosh, and Y. Grin, Phys. Rev. B **77**, 094421 (2008).

[47] K. Matsuhira, C. Sekine, M. Wakeshima, Y. Hinatsu, T. Namiki, K. Takeda, I. Shirotani, H. Sugawara, D. Kikuchi, and H. Sato, J. Phys. Soc. Jpn. **78**, 124601 (2009).

[48] G. P. Meisner, D. T. Morelli, S. Hu, J. Yang, and C. Uher, Phys. Rev. Lett. **80**, 3551 (1998).

[49] H. Kim, M. Kaviany, J. C. Thomas, A. Van der Ven, C. Uher, and B. Huang, Phys. Rev. Lett. **105**, 265901 (2010).

[50] H. Chi, H. Kim, J. C. Thomas, X. Su, S. Stackhouse, M. Kaviany, A. Van der Ven, X. Tang, and C. Uher, Phys. Rev. B **86**, 195209 (2012), URL `http://link.aps.org/doi/10.1103/PhysRevB.86.195209`.

[51] L. G. Akselrud, P. Y. Zavalii, Y. Grin, V. K. Pecharsky, B. Baumgartner, and E. Wölfel, Mater. Sci. Forum **133-136**, 335 (1993).

[52] G. M. Sheldrik, SHELXL-97, University of Göttingen, Göttingen (1997).

[53] V. F. Sears, Neutron News **3**, 26 (1992).

[54] M. M. Bredov, B. A. Kotov, N. M. Okuneva, V. S. Oskotskii, and A. L. Shakh-Budagov, Sov. Phys. Solid State **9**, 214 (1967).

[55] V. S. Oskotskii, Sov. Phys. Solid State **9**, 420 (1967).

[56] P. E. Bloechl, Phys. Rev. B **50**, 17953 (1994).

[57] P. Hohenberg and W. Kohn, Phys. Rev. **136**, B864 (1964).

[58] W. Kohn and L. J. Sham, Phys. Rev. **140**, A1133 (1965).

[59] G. Kresse and J. Furthmueller, Comput. Mater. Sci. **6**, 15 (1996).

[60] G. Kresse and D. Joubert, Phys. Rev. B **59**, 1758 (1999).

[61] J. P. Perdew, K. Burke, and M. Ernzerhof, Phys. Rev. Lett. **77**, 3865 (1996).

[62] J. P. Perdew, K. Burke, and M. Ernzerhof, Phys. Rev. Lett. **78**, 1396 (1997).

[63] F. Birch, Phys. Rev. **71**, 809 (1947), URL `http://link.aps.org/doi/10.1103/PhysRev.71.809`.

[64] K. Parlinski, *Neutrons and numerical methods N2M* (Am. Inst. Phys. Conference Proceedings 479, 1999).

[65] K. Parlinski, Z.-Q. Li, and Y. Kawazoe, Phys. Rev. Lett **78**, 4063 (1997).

[66] A. Kontio and E. D. Stevens, Acta Cryst. A **38**, 623 (1982).

[67] M. Jahnátek, M. Krajčí, and J. Hafner, Phys. Rev. B **71**, 024101 (2005), URL `http://link.aps.org/doi/10.1103/PhysRevB.71.024101`.

[68] J. Wang, S.-L. Shang, Y. Wang, Z.-G. Mei, Y.-F. Liang, Y. Du, and Z.-K. Liu, Calphad **35**, 562 (2011), ISSN 0364-5916, ¡ce:title¿World Round Robin Seminar 2010¡/ce:title¿, URL `http://www.sciencedirect.com/science/article/pii/S036459161100099X`.

[69] T. Dahm and K. Ueda, Phys. Rev. Letters **99**, 187003 (2007).

[70] M. J. Kangas, D. C. Schmitt, A. Sakai, S. Nakatsuji, and J. Y. Chan, Journal of Solid State Chemistry **196**, 274 (2012).

[71] O. Moze, L. Tung, J. Franse, and K. Buschow, Journal of Alloys and Compounds **268**, 39 (1998), ISSN 0925-8388, URL `http://www.sciencedirect.com/science/article/pii/S0925838897005860`.

[72] S. Christensen, L. Bjerg, A. Kaltzoglou, F. Juranyi, T. Fssler, T. Unruh, and M. Christensen, Journal of Applied Physics **113**, 084902 (2013).

[73] E. Shoko, Y. Okamoto, G. J. Kearley, V. K. Peterson, and G. J. Thorogood, Journal of Applied Physics **115**, 033703 (2014), URL `http://scitation.aip.org/content/aip/journal/jap/115/3/10.1063/1.4861641`.

[74] S. Samson, Acta Crystallographica **11**, 851 (1958), URL `http://dx.doi.org/10.1107/S0365110X58002425`.

[75] P. J. Brown, Acta Cryst. **10**, 133 (1957).

[76] P. I. Kripyakevich and O. S. Zarechnyuk, Dopov. Akad. Nauk. Ukr. RSR, Ser. A **30**, 364 (1968).

[77] M. Jahnatek, M. Krajci, and J. Hafner, Journal of Physics: Condensed Matter **15**, 5675 (2003).

[78] V. M. T. Thiede, W. Jeitschko, S. Niemann, and T. Ebel, Journal of Alloys and Compounds **267**, 23 (1998).

TABLE I. Nuclear coherent σ_{coh} and incoherent σ_{inc} neutron scattering cross sections in barns, masses in a.m.u., and total scattering power σ_{tot}/a.m.u. of the compounds' constituents.

element	σ_{coh}	σ_{inc}	σ_{tot}	a.m.u.	σ_{tot}/a.m.u.
Al	1.495	0.008	1.503	26.982	5.570
V	0.018	5.08	5.1	50.942	10.011
Sc	19	4.5	23.5	44.956	52.273
La	8.53	1.13	9.66	138.91	6.954
Ce	2.94	0.00	2.94	140.12	2.098

TABLE II. Physical properties from computer calculations and x–ray diffraction experiments. Lattice parameters are derived from powder (a') and single crystal (a^*) x–ray diffraction, by matching the volume dependent DFT calculations ($a_\circ$) with the Birch–Murnaghan EoS, and from DFT optimized structures (a). Bulk modulus $B_\circ$ and its pressure derivative B' are obtained by matching the EoS. Compounds are characterized by the occupants of the 8a site.

	□	Sc	La	Ce
a' [Å]	14.5121(3)	14.4936(8)	14.6126(6)	14.5570(7)
a^* [Å]	14.5125(7)	14.5057(7)	–	–
$a_\circ$ [Å]	14.4378(3)	14.4303(3)	14.5805(3)	14.512(2)
$B_\circ$ [GPa]	86.02(6)	91.470(3)	88.77(5)	91.9(2)
B' [GPa]	4.34(2)	4.32(1)	4.35(2)	4.45(8)
a [Å]	14.4135	14.4068	14.5601	14.4870

TABLE III. Crystallographic data (structure type $Mg_3Ge_2Al_{18}$–variant[74–76], space group $Fd\bar{3}m$ (227), origin choice 2) obtained for the DFT optimized structures and derived from x–ray experiments on polycrystalline and single–crystal specimen. Listed are fractional coordinates x y z of the cation sites. The fractional coordinates for Al(16c), A(8a), and V(16d) correspond to (0 0 0), (1/8 1/8 1/8), and (1/2 1/2 1/2) respectively. Compounds are characterized by the occupants of the 8a site.

		DFT calculation			powder x–ray			single crystal x–ray		
		x	y	z	x	y	z	x	y	z
□	Al(48f)	0.4849	1/8	1/8	0.4857(2)	1/8	1/8	0.48506(5)	1/8	1/8
	Al(96g)	0.0599	x	0.3227	0.0613(1)	x	0.3221(8)	0.05982(2)	0.05982(2)	0.32304(4)
Sc	Al(48f)	0.4858	1/8	1/8	0.4854(3)	1/8	1/8	0.4858(1)	1/8	1/8
	Al(96g)	0.0595	x	0.3239	0.0596(4)	x	0.3267(3)	0.0596(1)	x	0.3236(1)
La	Al(48f)	0.4872	1/8	1/8	0.4864(3)	1/8	1/8			
	Al(96g)	0.0585	x	0.3263	0.0596(4)	x	0.3267(3)			
Ce	Al(48f)	0.4875	1/8	1/8	0.4866(3)	1/8	1/8			
	Al(96g)	0.0590	x	0.3252	0.0589(4)	x	0.3254(3)			

TABLE IV. Frequencies $\omega_{\mathrm{i}}^{\circ}$ in TeraHertz of the vibrational eigenstates at the Γ−point obtained for $A\mathrm{V}_2\mathrm{Al}_{20}$ ($A = \square$, Sc, La, and Ce). They are grouped according to the symmetry of the eigenstates. Their multiplicity and their activity in respect to infrared (I) and Raman (R) scattering are indicated with their symmetries.

	$\square V_2Al_{20}$	ScV_2Al_{20}	LaV_2Al_{20}	CeV_2Al_{20}
T1u(I)	0.0	0.0	0.0	0.0
T1u(I)	3.727	1.894	3.023	3.234
T1u(I)	4.133	4.108	3.288	3.824
T1u(I)	4.830	4.903	5.082	5.165
T1u(I)	5.991	5.913	6.018	6.103
T1u(I)	6.642	6.297	6.752	6.676
T1u(I)	7.583	6.861	7.239	7.045
T1u(I)	7.844	7.432	7.359	7.325
T1u(I)	8.529	7.683	7.514	7.505
T1u(I)	9.626	8.604	8.254	8.311
T1u(I)	11.392	9.599	9.392	9.420
T1u(I)	12.681	10.952	10.263	10.463
T1u(I)		12.896	12.438	12.629
T2g(R)	4.313	2.001	3.186	3.157
T2g(R)	5.309	4.723	4.905	4.927
T2g(R)	6.270	5.487	5.613	5.563
T2g(R)	7.042	6.533	6.507	6.508
T2g(R)	9.014	7.399	7.384	7.393
T2g(R)	9.218	9.007	8.758	8.833
T2g(R)	10.230	9.358	8.906	9.025
T2g(R)	12.105	10.048	9.476	9.617
T2g(R)		12.169	11.723	11.804
Eg(R)	4.014	4.262	4.510	4.500
Eg(R)	6.142	6.113	5.938	6.031
Eg(R)	7.884	8.303	8.210	8.283
Eg(R)	10.419	10.043	9.438	9.612
A1g(R)	7.723	7.741	7.748	7.911
A1g(R)	9.494	9.330	8.750	9.016
A1g(R)	12.145	11.406	10.684	10.900
T2u	2.734	2.735	2.662	2.895
T2u	3.915	3.838	3.147	3.650
T2u	4.575	4.526	4.671	4.682
T2u	5.815	5.682	5.660	5.693
T2u	6.064	6.277	6.432	6.335
T2u	7.324	7.101	7.336	7.220
T2u	8.391	8.238	8.080	8.186
T2u	11.457	11.603	11.206	11.284
T1g	3.503	3.637	3.570	3.755
T1g	4.752	4.722	4.876	4.872
T1g	4.869	4.974	5.132	5.064
T1g	6.749	7.045	6.916	7.021
T1g	7.290	7.215	7.436	7.281
T1g	10.544	10.663	10.326	10.374
Eu	3.876	3.698	2.782	3.345
Eu	4.315	4.427	4.571	4.569
Eu	5.587	5.940	5.597	5.847
Eu	7.760	7.023	6.817	6.741
Eu	8.302	8.741	8.697	8.695
Eu	10.043	9.582	8.879	9.024
A2u	3.840	5.772	7.021	6.694
A2u	7.389	7.661	7.484	7.424
A2u	8.892	8.492	7.716	7.816
A2u	9.767	9.132	8.702	8.949
A2u	11.975	11.659	10.909	11.083
A2g	2.902	2.741	2.705	2.757
A1u	4.902	5.093	5.411	5.331

TABLE V. Mean energy $\overline{E}_\mathrm{n}$ and the variance $\widetilde{E}_\mathrm{n}$ of the partial spectral densities $Z_\mathrm{n}(\omega)$ of Al(16c) and A(8a), and averaged sound velocities v_av and Debye temperaturesv Θ_D computed from $Z(\omega)$. Compounds are characterized by the occupants of the 8a site.

	□	Sc	La	Ce
$\overline{E}_\mathrm{Al(16c)}$ [meV]	16.8	18.9	18.1	19.7
$\widetilde{E}_\mathrm{Al(16c)}$ [meV^2]	12.8	28.4	69.2	45.0
$\overline{E}_{A\mathrm{(8a)}}$ [meV]	–	9.0	13.8	13.6
$\widetilde{E}_{A\mathrm{(8a)}}$ [meV^2]	–	33.6	28.7	21.1
v_av [m/s]	4866	4420	4641	4726
Θ_D [K]	563	520	540	551

TABLE VI. Fit parameters A in eV/Å^2 and B in eV/Å^4 from approximating the atomic potentials as $U(\Delta x) = A\Delta x^2 + B\Delta x^4$. Subscripts with A and B denote the approximated directions and superscripts the potentials.

Compound	A^Al_{x00}	B^Al_{x00}	A^Al_{xxx}	B^Al_{xxx}	A^M_{x00}	B^M_{x00}	A^M_{xxx}	B^M_{xxx}
□V_2Al_{20}	0.9420(3)	1.102(6)	0.84(2)	0.0	–	–	–	–
ScV_2Al_{20}	1.24	0.861(2)	1.834(1)	0.756(7)	0.610(1)	2.03(1)	0.61(3)	2.1(4)
LaV_2Al_{20}	1.284(1)	0.63(2)	2.71	1.0186(1)	3.624(1)	1.367(2)	3.624(1)	1.5(1)
CeV_2Al_{20}	1.395(6)	0.64(9)	2.495(4)	0.98(7)	3.441(5)	1.22(7)	3.44(2)	1.3(3)

TABLE VII. Force constants F_ii and F_ij $(\mathrm{i}, \mathrm{j} = \mathrm{x}, \mathrm{y}, \mathrm{z})$ of Al(16c) and A(8a) in eV/Å^2 as calculated from the Hellmann–Feynman forces.

Compound	$F^\mathrm{Al(16c)}_\mathrm{ii}$	$F^\mathrm{Al(16c)}_\mathrm{ij}$	$F^{A\mathrm{(8a)}}_\mathrm{ii}$
□V_2Al_{20}	1.897	-0.100	–
ScV_2Al_{20}	2.489	0.594	1.234
LaV_2Al_{20}	2.571	1.423	7.266
CeV_2Al_{20}	2.792	1.096	6.885

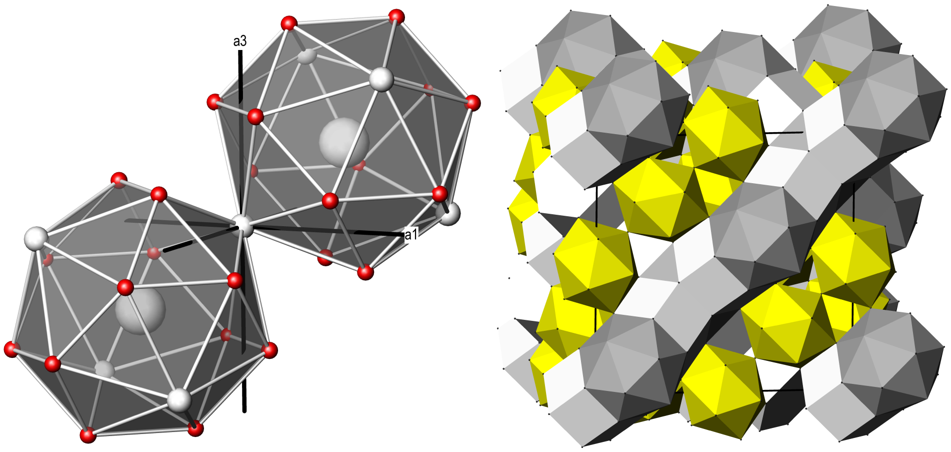

FIG. 1. (Color online) Left, environment of the *A* filler atoms at the center of the 16 vertices Friauf polyhedra formed by Al(96g) (small red balls) and Al(16c) (medium white balls) atoms. The crystallographic axes are indicated with a1 corresponding to x-direction and a3 to z-direction, respectively. Right, polyhedral representation of cubic AV_2Al_{20} with the distorted Al(48f) icosahedra centered by V atoms (yellow) surround hexagonal Al(96g) prisms (white) which are centered by Al(16c). They nest the Friauf polyhedra centered by *A*.

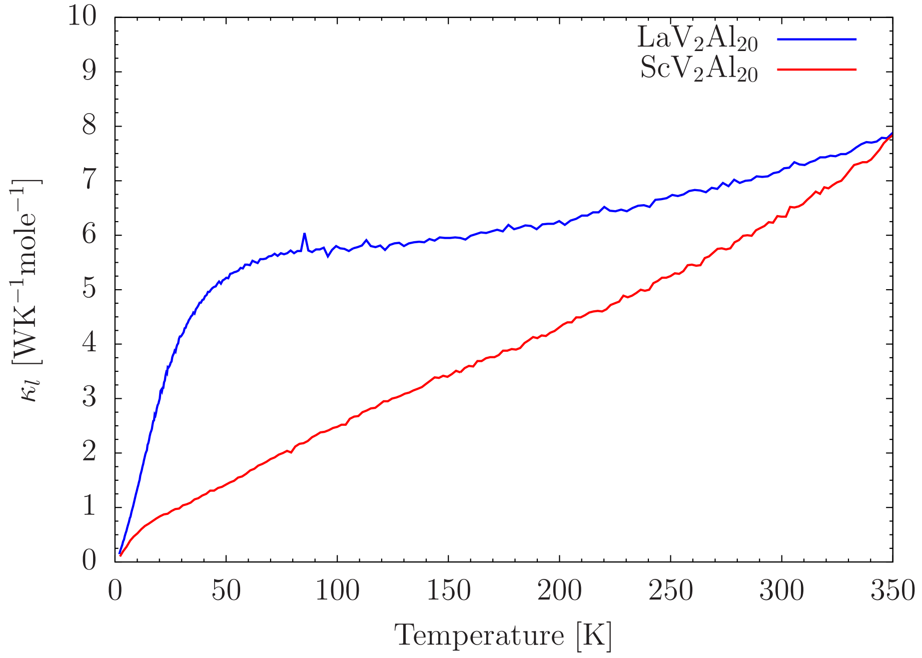

FIG. 2. (Color online) Lattice thermal conductivity of ScV_2Al_{20} and LaV_2Al_{20}.

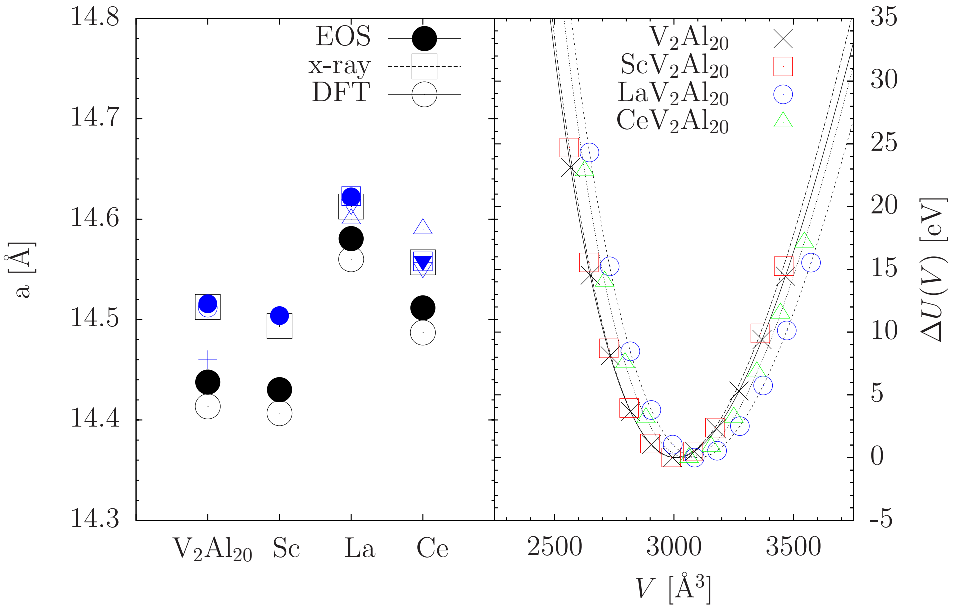

FIG. 3. Left, lattice parameters a of $A\mathrm{V_2Al_{20}}$ compounds derived from EoS data (large •), x–ray scattering results (large □), and DFT optimized structures (large ○) The ternary compounds are characterized by the occupants of the 8a site. Literature data are reported as small symbols. They are extracted from Refs. 24 and 25 (small •), 22 (small ○), 77 (+), 70 (□), 76 (△), 78 (▽), 71 (▼). Right, energy difference dependent on cell volume. Lines correspond to fit results of the Birch–Murnaghan equation of state indicated as eq. 1.

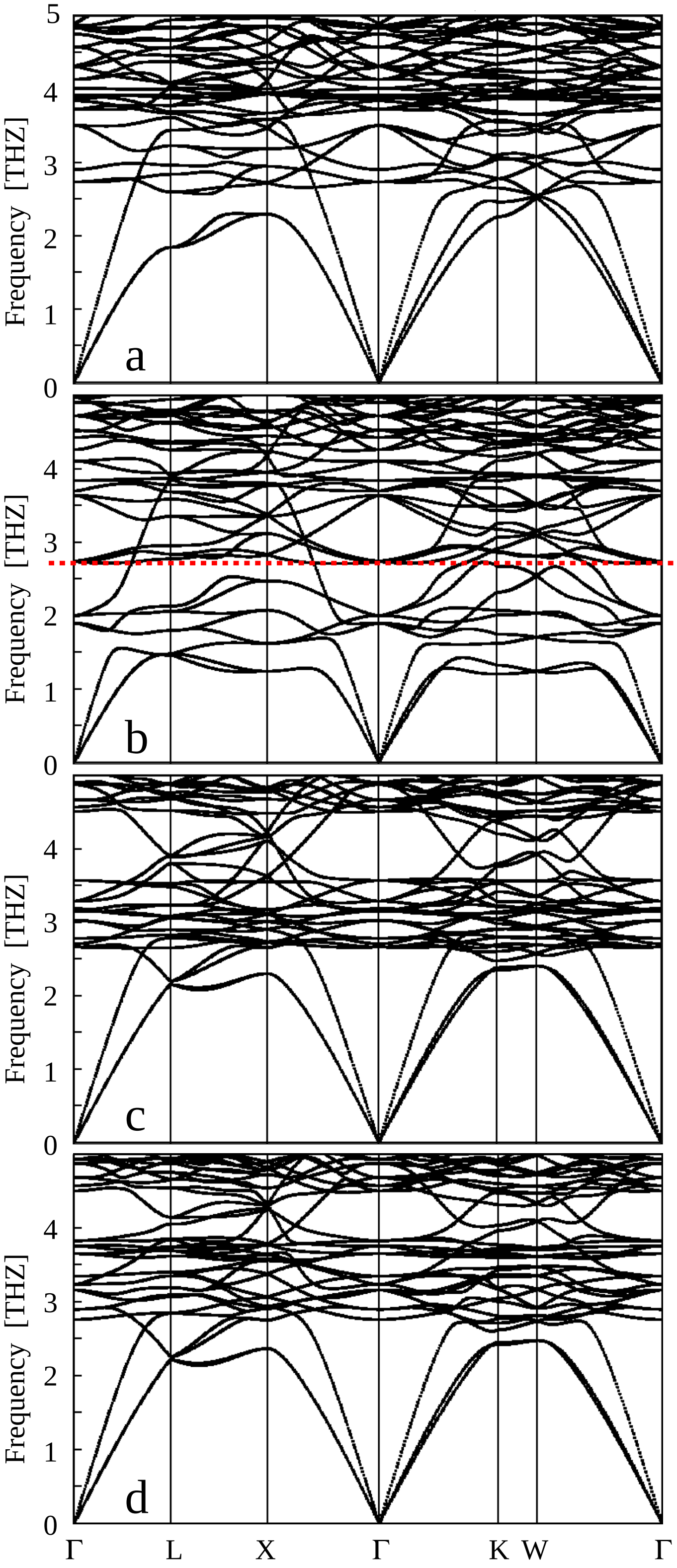

FIG. 4. Phonon dispersion relations computed for the compounds □V_2Al_{20} (a), ScV_2Al_{20} (b), LaV_2Al_{20} (c), and CeV_2Al_{20} (d). Red dashed line with ScV_2Al_{20} data indicates the energy below which the weakly dispersive modes are dominated by the amplitudes of Sc vibrations.

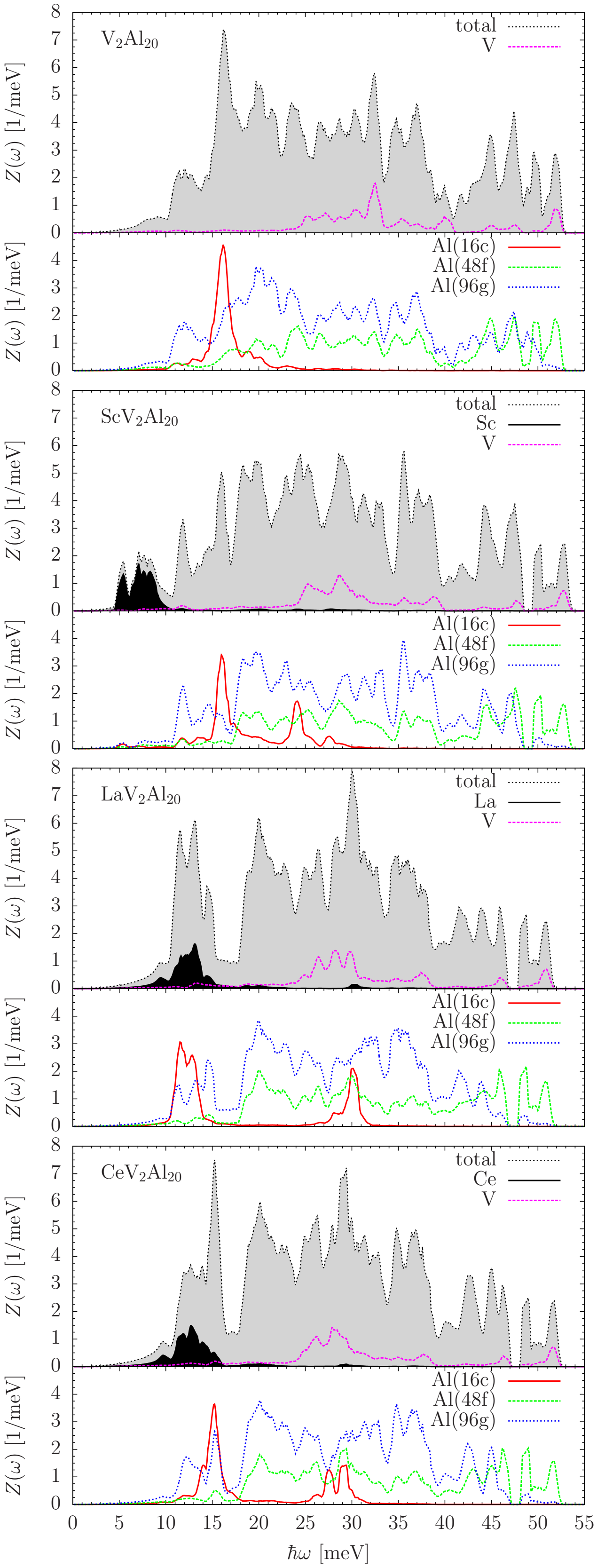

FIG. 5. (Color online) Total and partial densities of states of AV_2Al_{20} with $A = \square$, Sc, La and Ce. Linestyle and color scheme are indicated in the figures. Gray and black shaded areas highlight the total $Z(\omega)$ and the partial contribution $Z_{A(8a)}(\omega)$.

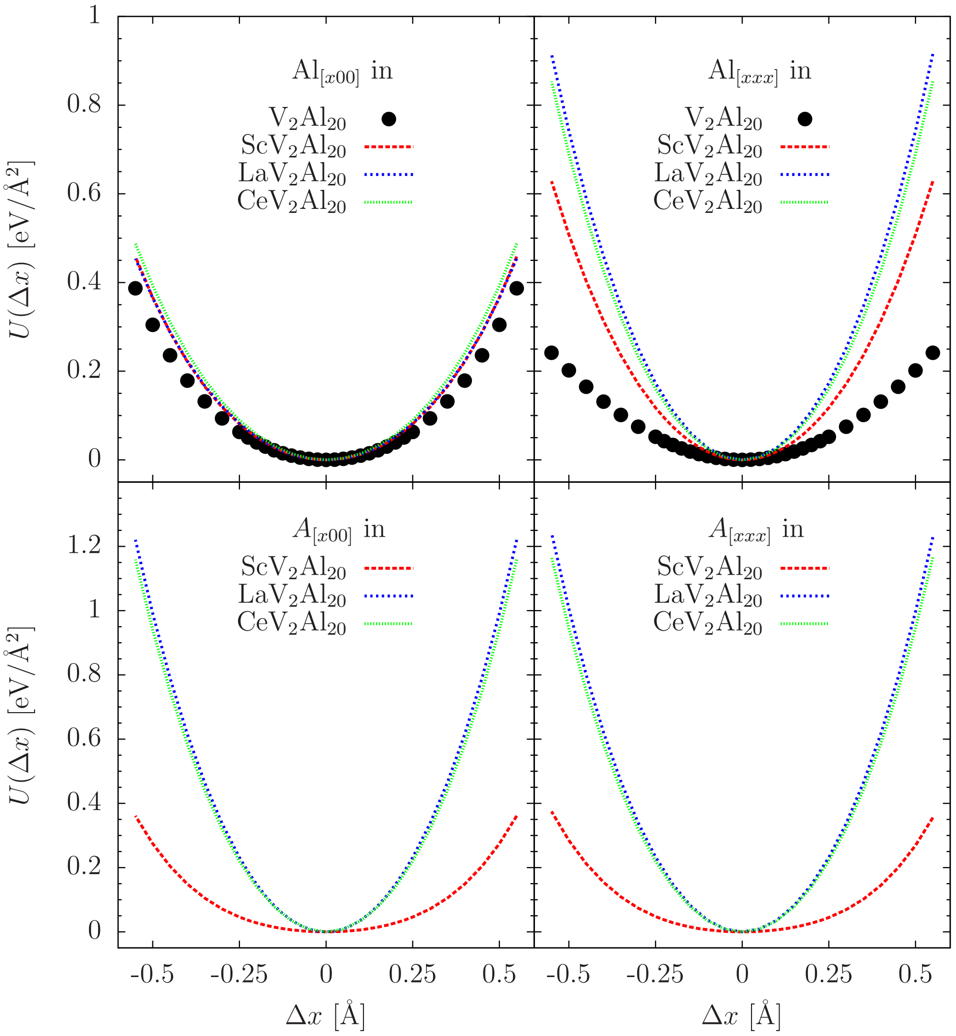

FIG. 6. Atomic potentials $U(\Delta x)$ of Al(16c) and A(8a) computed from DFT in the directions $x00$ and xxx.

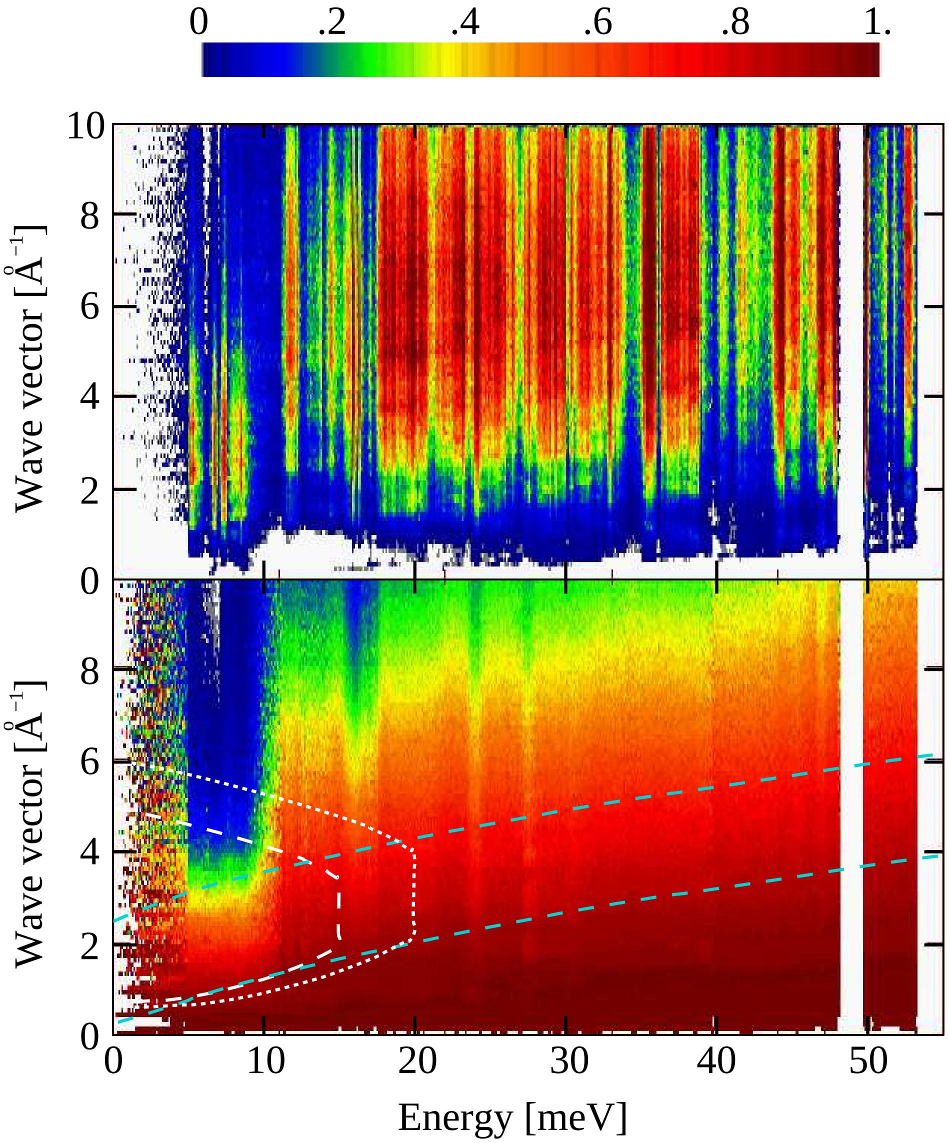

FIG. 7. (Color online) Top, contrast plot of the PALD derived phonon formfactor $F(\mathbf{Q}, \omega, T = 300\ \mathrm{K})$ of $\mathrm{ScV_2Al_{20}}$. Bottom, contrast plot of the relative Debye–Waller factor $F(\mathbf{Q}, \omega, T = 300\ \mathrm{K})/F(\mathbf{Q}, \omega, T = 1\ \mathrm{K})$ of $\mathrm{ScV_2Al_{20}}$. Lines render the phase–spaces covered by the IN4@ILL Stokes–line experiments with $\lambda_\mathrm{i} = 1.8$ Å (white dotted line) and 2.2 Å (white dashed line), and by the IN6@ILL anti–Stokes–line measurements (cyan dashed lines) with $\lambda_\mathrm{i} = 4.14$ Å.

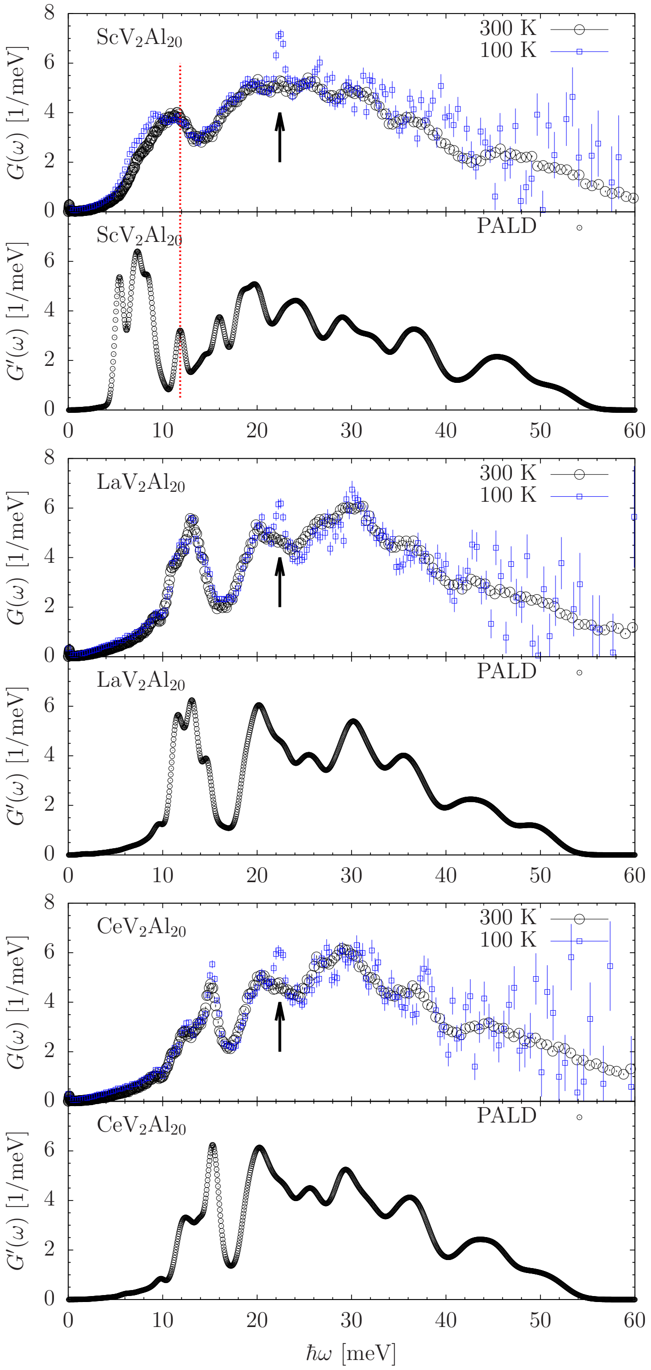

FIG. 8. (Color online) Generalized density of states $G(\omega)$ of ScV$_2$Al$_{20}$, LaV$_2$Al$_{20}$, and CeV$_2$Al$_{20}$. Top, derived from INS measurements at IN6@ILL at T = 100 and 300 K. Bottom, derived from PALD data calculated within the harmonic approximation for = 300 K. Red dotted line with ScV$_2$Al$_{20}$ data highlights the first peak showing a classical anharmonic T dependence. Arrows indicate a peak due to elastic second–order scattering from the monochromator detectable at low T.

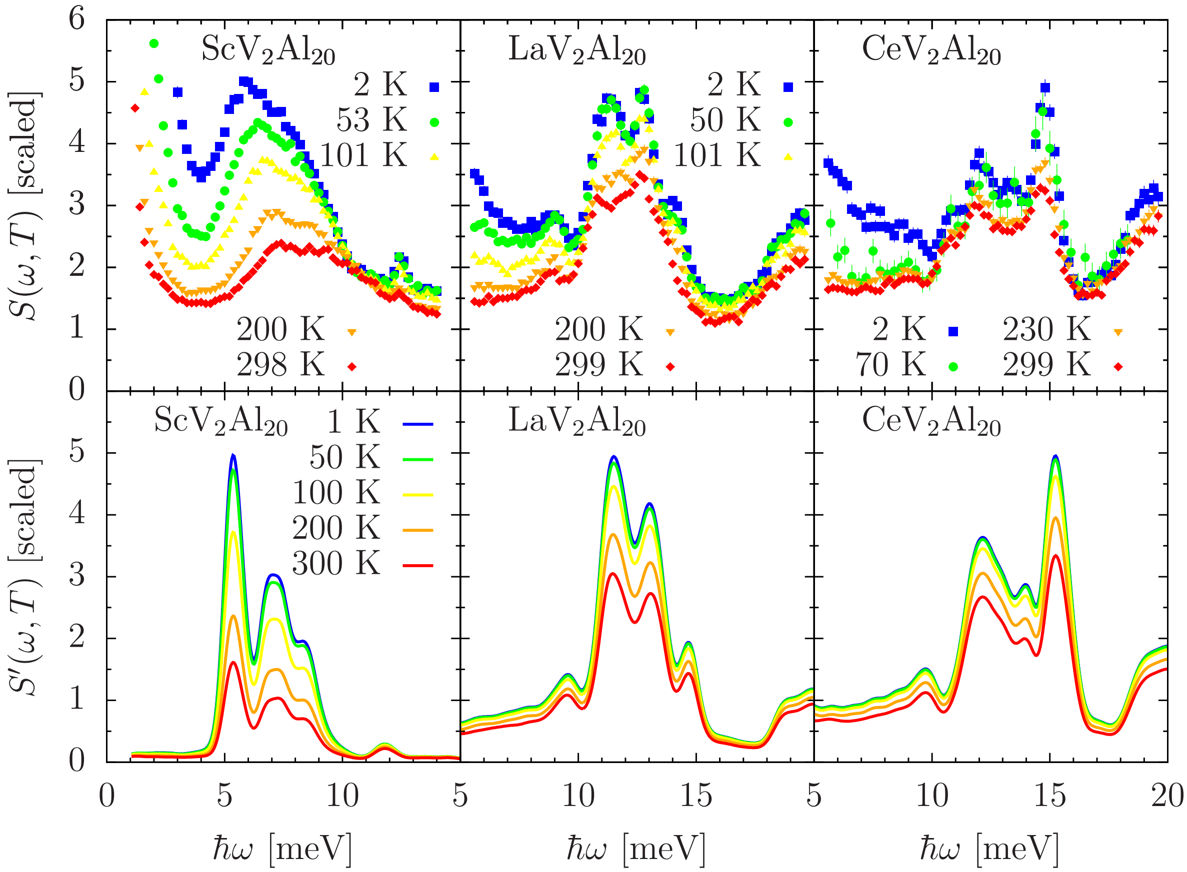

FIG. 9. (Color online) Measured (top panel) and PALD–calculated (bottom panel) dynamic structure factors of ScV$_2$Al$_{20}$, LaV$_2$Al$_{20}$, and CeV$_2$Al$_{20}$. Temperatures applied during measurements are indicated in the corresponding subfigures. PALD data have been calculated for the same T reported with the ScV$_2$Al$_{20}$ results.

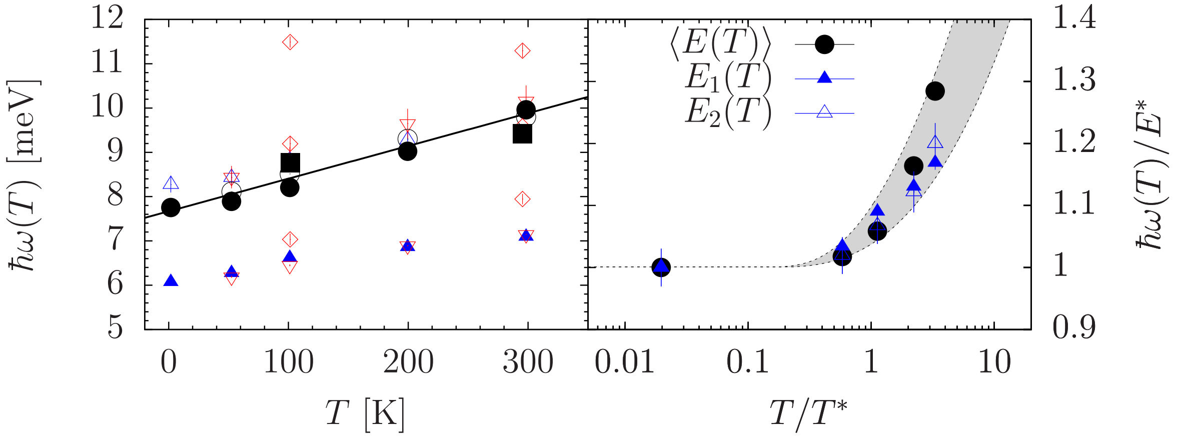

FIG. 10. Left, temperature dependence of the characteristic low–energy peaks in the inelastic response of ScV_2Al_{20}. Large symbols represent the momenta $\langle E(T)\rangle$ of the approximated spectral density derived from IN4@ILL Stokes line (•), anti–Stokes line (○), and IN6@ILL anti–Stokes line (■). The two characteristic energies $E_1(T)$ and $E_2(T)$ identified in the Stokes line of IN4@ILL data are discriminated by △ and ▲, respectively. Anti–Stokes line data are characterized by ▽ for IN4@ILL data and ♢ for IN6@ILL data. Full line represents a linear fit to all $\langle E(T)\rangle$ data. Right, comparison of the characteristic energies with the anharmonic model by Dahm and Ueda of Ref. 69. Gray shaded area is given by the anharmonicity parameter $0.15 \leq \beta \leq 0.5$.

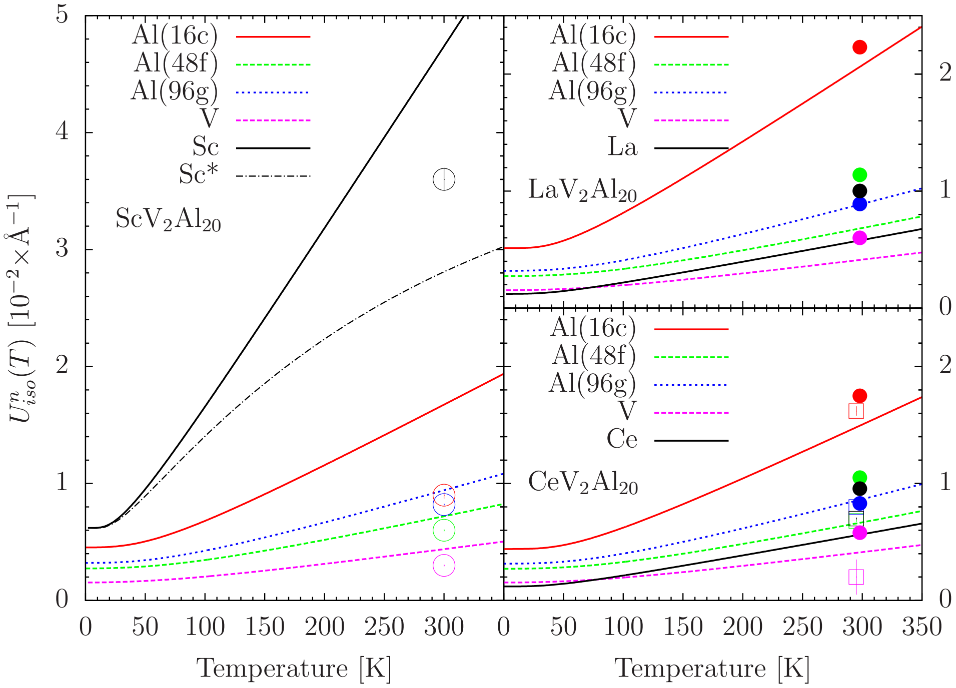

FIG. 11. (Color online) Atomic thermal displacement parameters $U^{\rm n}_{\rm iso}(T)$ computed from partial $Z_{\rm n}(\omega)$ within the harmonic approximation. Linestyle and color schemes are indicated in the subfigures. Symbols report literature data derived from single crystal diffraction experiments by Kangas et al. (•) in Ref. 70, Moze et al. (□) in Ref. 71 and in this work (large ○). Corresponding color schemes are chosen. Additional $U^{\rm Sc}_{\rm iso}(T)$ was computed for scandium corrected for the anharmonic temperature shift (Sc*) from $Z_{\rm Sc}[\omega(T)]$.

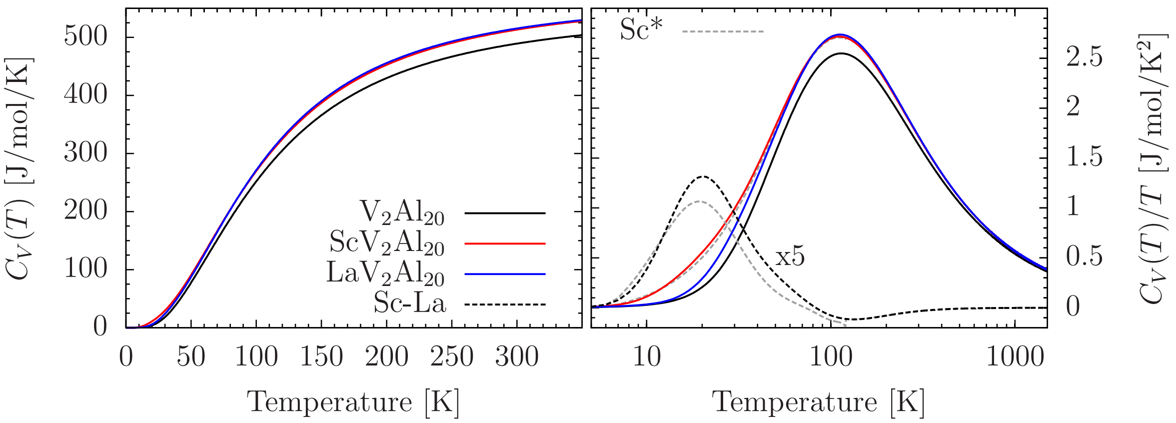

FIG. 12. (Color online) Left, heat capacities $C_V(T)$ calculated from DFT and LDC $Z(\omega)$ within the harmonic approximation. Right, low–T region is highlighted as $C_V(T)/T$. The color code valid for both subfigures is indicated with $C_V(T)$ data. Additional $C_V(T)/T$ was computed with $Z[\omega(T)]$ corrected for the anharmonic temperature shift (Sc*) of Sc–dominated modes.

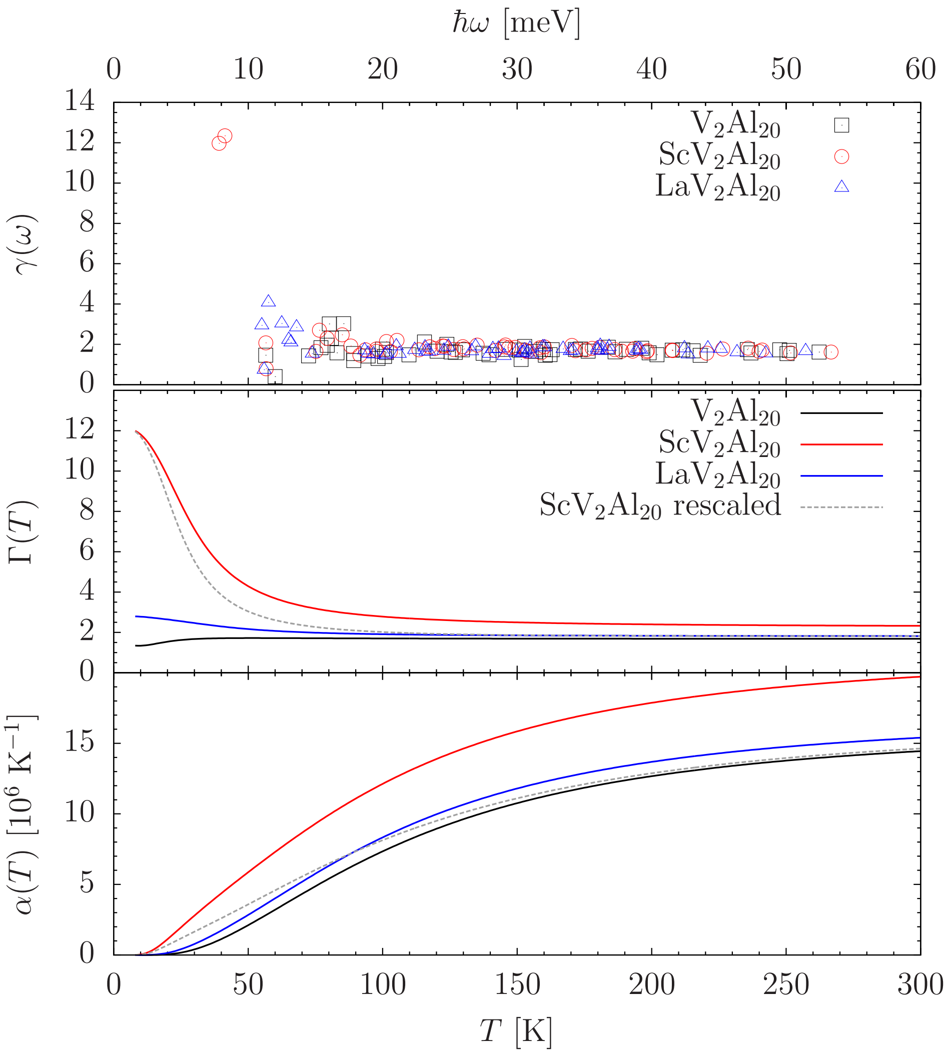

FIG. 13. (Color online) From top to bottom, mode Grüneisen parameter $\gamma(\omega_\mathrm{i})$, thermodynamic Grüneisen parameter $\Gamma(T)$, and coefficient of linear expansion $\alpha(T)$ of □V_2Al_{20}, ScV_2Al_{20}, and LaV_2Al_{20}.